Chapter 3
Continuum Approximations

Joseph E. Bishop and Hojun Lim

3.1 Introduction

In continuum mechanics, instead of using discrete sums to assemble forces and assess equilibrium, as in molecular dynamics or dislocation dynamics, one instead uses the machinery of differential and integral calculus to cast Newton's second law in the form of a set of partial-differential equations, the solution of which gives the equilibrium configuration of the entire collection of discrete entities. While seemingly inapplicable to nanoscale structures, the use of continuum mechanics at the nanoscale is still a useful approximation with careful consideration of the assumptions inherent in the theory and with the inclusion of scale-dependent physical phenomena such as surface effects, microstructural effects, and nonlocal phenomena. The current literature on these generalized continuum theories is large and ever growing. Our goal in this chapter is to give a brief introduction to continuum mechanics with a focus on nanomechanics and how the classical theory can be modified to include phenomena such as surface effects and microstructural effects. Numerous references are given to more detailed expositions.

Section 3.2 begins with a brief review of classical continuum mechanics, an overview of micromorphic continuum formulations, and concludes with a discussion of continuum formulations that include an explicit surface stress. This section is also helpful in understanding the quasi-continuum method presented in Chap. 5

J.E. Bishop (✉)
Sandia National Laboratories, Engineering Sciences Center, Albuquerque, NM 87185, USA
e-mail: jebisho@sandia.gov

H. Lim
Sandia National Laboratories, Materials Science and Engineering Center, Albuquerque, NM 87185, USA
e-mail: hnlim@sandia.gov

C.R. Weinberger, G.J. Tucker (eds.), *Multiscale Materials Modeling for Nanomechanics*, Springer Series in Materials Science 245,
DOI 10.1007/978-3-319-33480-6_3

of this book. At the center of continuum mechanics is homogenization theory which provides a mathematically elegant and rigorous framework for replacing a discrete collection of interacting entities by an equivalent homogenous continuum with effective material properties. Furthermore, given the continuum approximation of the system, homogenization theory provides a method for recovering the solution of the original discrete or heterogeneous system. These concepts are discussed in Sect. 3.3. Continuum approaches to modeling crystal-plasticity are discussed in Sect. 3.4. These continuum crystal-plasticity models explicitly incorporate descriptions of the active slip systems and hardening phenomena at the crystal scale.

Errors in a continuum approximation to a discrete system are unavoidable whenever the introduced length scales are comparable to the length scale of the discrete system. Generalized continuum theories may be able to reproduce qualitatively correct physical phenomenon, such as a surface effect or optical-branch phonon dispersion curves, but the accuracy of the continuum theory must be judged with respect to the true behavior of the original discrete system. Two simple one-dimensional examples are given in the Appendix to demonstrate errors induced in a continuum approximation of a discrete system.

There are several excellent books available that include detailed discussions, examples, and tutorials for many of the concepts presented in this chapter. The book "Applied Mechanics of Solids" by Bower [19] gives a thorough yet accessible coverage of numerous topics in solid mechanics including continuum mechanics, constitutive modeling at the crystalline scale, and the finite-element method. The book "Nonlinear Continuum Mechanics for Finite Element Analysis" by Bonet and Woods [18] gives an introduction to tensor analysis, large deformation continuum mechanics, inelastic constitutive modeling, and nonlinear finite-element analysis. The book "Nonlinear Finite Elements for Continua and Structures" by Beyltschko et al. [15] thoroughly covers these topics and contains a chapter on dislocation density-based crystal-plasticity. The book "Crystal Plasticity Finite Element Methods in Materials Science and Engineering" by Roters et al. [127] gives an introduction to continuum mechanics, the finite-element method, homogenization, and presents numerous concepts in crystal-plasticity. The book "Practical Multiscaling" by Fish [50] covers numerous topics in homogenization and multiscale modeling.

3.2 Continuum Approximations

The continuum approximation is a mathematical idealization for modeling the collective response, or state, of discrete systems. The continuum approximation is extremely efficient. The very large number of degrees of freedom required to describe the complete state of a macroscale discrete system, for example, an Avogadro's number, is instead approximated using differential, integral, and functional calculus. Mathematically, the vector space of real numbers (also called the continuum) is used to represent the physical domain of the system. The mathematical continuum is continuous (no gaps) and infinitely divisible. Spatial fields, such as displacement and stress, are then defined on this continuum using

familiar notions of a function. Finite differences and finite sums within the physical system are approximated with function derivatives and integrals, respectively. The approximation of a discrete system using differential and integral calculus is, operationally, the dual of approximating a continuous mathematical model using finite differences and finite sums; errors induced in the former are similar to the errors induced in the latter.

The classical continuum theory [90] does not contain an intrinsic length scale. One ramification for solid mechanics is that, for a given boundary-value problem, the stress and strain fields do not change when the physical dimensions change. The classic example from solid mechanics is that of a "hole in a plate." For the case of a homogeneous isotropic linear-elastic continuum, an infinite plate containing a circular hole subjected to far field uniaxial tension has a maximum stress around the hole that is exactly three times larger than the far field stress [146]. In the classical continuum theory, this stress ratio is independent of the size of the hole; a meter-sized hole for a geotechnical application gives the same stress concentration as a nanometer-sized hole in a nanotechnology application. This result is nonphysical. For a physical material, there is always an intrinsic length scale, for example, either the atomic spacing, size of a unit cell, or grain size for a polycrystalline material. When the size of the hole approaches these intrinsic length scales, the assumptions inherent in the continuum formulation are increasingly in error [40, 61, 101]. This error is clearly seen in the wave-propagation/phonon dispersion curves. The classical theory predicts no dispersion, while a discrete system will display a very complex dispersion response including both acoustical and optical branches [26, 27, 31].

Furthermore, classical continuum theory does not predict the existence of a surface effect. Surface effects, including edge and vertex effects, arise in atomic systems fundamentally due to the difference in the coordination number of atoms near the surface versus atoms in the interior and due to long-range atomic forces beyond nearest-neighbor interactions. These in turn lead to differences in the charge distributions, bond lengths, and bond angles near the surface versus the interior [67, 113, 114, 152]. Manifestations of the surface effect include surface tension in liquids as well as surface and interfacial stresses in solids [23, 57–60, 108, 130]. Surface effects can produce exotic physical behavior of both liquids and solids, such as capillarity, adsorption, and adhesion [24, 67]. Surface and interface stresses can also modify the local and far field deformations of nanoscale structures [40, 61, 96, 100, 131, 134]. Homogenization theory of periodic media also predicts the existence of a surface effect due to the difference in material confinement at the surface as compared to the interior [11, 39, 41]. This will be discussed in Sect. 3.3.

Several physically motivated generalizations to classical continuum theory have been proposed that introduce both a physical length scale and surface effects. These include the micromorphic theory of Mindlin [102] and Eringen [45, 48, 55, 140], the nonlocal theories [46, 47, 78] including peridynamics [136–138], and surface-stress formulations of Gurtin [57–60]. The micromorphic theory introduces additional microstructural degrees of freedom within a unit cell that result in a strain-gradient

effect in the governing equilibrium equations. The classical theory is reproduced when the size of unit cell is reduced to zero, or in the long wave-length limit. Nonlocal theory has its foundations in the long-range interactions of interatomic forces. These theories posit that the constitutive response at a material point is dependent on the state in a nonlocal region around the point, unlike in classical theories. Strain-gradient theories can be viewed as special cases of the nonlocal formulations [3, 120, 124]. Homogenization theory of periodic media also predicts the existence of strain-gradient effects whenever the unit cell is finite [30, 139, 149, 154]. This will be discussed in Sect. 3.3.

It is important to keep in mind that these generalized continuum theories are still only approximations of the original discrete system. Errors in a continuum approximation to a discrete system are unavoidable whenever the introduced length scales are comparable to the length scale of the discrete system. The generalized theories may be able to reproduced qualitatively correct physical phenomenon, such as a surface effect or optical-branch phonon dispersion curves, but the accuracy of the continuum theory must be judged with respect to the true behavior of the original discrete system. For example, the surface effect may occur only over a few atomic spacings normal to the surface, while the governing equilibrium equations are still in the form of partial-differential equations. Examples are presented in the Appendix in order to demonstrate errors in the continuum approximation.

The classical theory of continuum mechanics is very briefly reviewed in Sect. 3.2.1. The micromorphic theories are briefly presented in Sect. 3.2.2. The surface-stress formulations are briefly presented in Sect. 3.2.3. The nonlocal theories are summarized in Sect. 3.2.4.

3.2.1 Classical Theory

There are many excellent texts on classical continuum mechanics [18, 19, 64, 83, 90]. In this section we give a very brief overview of the standard theory. We use primarily index notation, but also use vector notation for clarity when needed. Thus, x_i represents the three components ($i = 1, 2, 3$) of the vector $\mathbf{x}$. The summation convention of repeated indices within a product or quotient will also be used, for example, $x_i x_i = x_1 x_1 + x_2 x_2 + x_3 x_3$.

Consider the motion of a body $\mathscr{B}$ with interior domain Ω and boundary Γ subjected to a body force b_i per unit volume and applied surface tractions t_i. A Lagrangian description of the motion of $\mathscr{B}$ is used. The current position of a material point is given by x_i, and the original position is given by X_i. The displacement field is given by $u_i = x_i - X_i$. Since the spatial position of a material point is a function of it's original position $x_i(X_j)$, we can define the (material) derivative of the current position with respect to the original position, $\partial x_i / \partial X_j$. This vector derivative is called the deformation gradient, denoted by F_{ij}, and is one of the primary quantities used in continuum solid mechanics to describe the deformation of the body (kinematics). In terms of displacement,

$$F_{ij} = \partial u_i / \partial X_j + \delta_{ij} \, . \tag{3.1}$$

where δ_{ij} is the Kronecker delta with $\delta_{ij} = 1$ if $i = j$ and $\delta_{ij} = 0$ if $i \neq j$. From the deformation gradient, one can define measures of strain, for example, engineering strain, logarithmic strain, and Green strain [18]. For example, the Green strain tensor E_{ij} (also called the Lagrangian strain tensor) is defined as [18]

$$E_{ij} \doteq \frac{1}{2} \left(F_{ki} F_{kj} - \delta_{ij} \right) \, . \tag{3.2}$$

The physical interpretation of E_{ij} may be obtained by noting that it describes how the inner product between two infinitesimal material vectors, $d\mathbf{X}_1$ and $d\mathbf{X}_2$, change under deformation to $d\mathbf{x}_1$ and $d\mathbf{x}_2$, respectively,

$$\frac{1}{2} \left(d\mathbf{x}_1 \cdot d\mathbf{x}_2 - d\mathbf{X}_1 \cdot d\mathbf{X}_2 \right) = d\mathbf{X}_1 \cdot \mathbf{E} \, d\mathbf{X}_2 \, . \tag{3.3}$$

For the special case of $d\mathbf{X}_1 = d\mathbf{X}_2 = d\mathbf{X}$, and consequently $d\mathbf{x}_1 = d\mathbf{x}_2 = d\mathbf{x}$, Eq. (3.3) becomes

$$\frac{1}{2} \left(dl^2 - dL^2 \right) = d\mathbf{X} \cdot \mathbf{E} \, d\mathbf{X} \, , \tag{3.4}$$

where $(dl)^2 \doteq d\mathbf{x} \cdot d\mathbf{x}$ and $(dL)^2 \doteq d\mathbf{X} \cdot d\mathbf{X}$. Dividing by $(dL)^2$ gives the scalar version (uniaxial) of the Green strain,

$$\frac{dl^2 - dL^2}{2(dL)^2} = \frac{d\mathbf{X}}{dL} \cdot \mathbf{E} \frac{d\mathbf{X}}{dL} = \mathbf{N} \cdot \mathbf{E} \, \mathbf{N} = N_i E_{ij} N_j \, , \tag{3.5}$$

where $\mathbf{N}$ is a unit material vector in the direction of $d\mathbf{X}$. The full inner-product version given in Eq. (3.3) indicates that the strain tensor $\mathbf{E}$ contains both shear and normal strains, presented here in a large deformation formulation.

In order to describe the kinetics of the material, we need to derive both measures of stress and the constitutive relations between stress and strain. In the context of hyperelasticity, one posits a potential energy function W of the strain tensor,

$$W = W(\mathbf{E}) \, . \tag{3.6}$$

Certain restrictions are placed on W to obtain a constitutive model that is independent of the observer (objectivity) and to obtain a stable material. A stress tensor $\mathbf{S}$, called the second Piola–Kirchhoff stress, is defined to be work conjugate to the derivative of W with respect to the strain $\mathbf{E}$,

$$S_{ij} = \frac{\partial W}{\partial E_{ij}} \tag{3.7}$$

so that

$$dW = \mathbf{S} : d\mathbf{E} = S_{ij}\, dE_{ij} \ . \tag{3.8}$$

In many macroscale constitutive models, phenomenological formulations are developed for specific classes of materials such as those for plasticity and viscoplasticity (polycrystalline metals) [74, 83, 87, 111], hyperelasticity and viscoelasticity (polymers) [29], pressure dependent plasticity (porous materials) [5, 19]. These models use various internal-state variables to phenomenologically model physical effects such as dislocation slip, dislocation density, porosity, and damage. Through these constitutive models, the stress measure is related to the entire history of deformation. Constitutive models also exist at the single-crystal level [127]. Section 3.4 gives an overview of continuum crystal-plasticity modeling.

In the special case of small-deformation linear elasticity,

$$S_{ij} = C_{ijkl} E_{kl} \ , \tag{3.9}$$

where C_{ijkl} is the fourth-order elasticity stiffness tensor with $3^4 = 81$ components. For the special case of infinitesimal displacements, the various stress and strain measures are equivalent, and it is common to express the linear relation between stress and strain in Eq. (3.9) using the Cauchy stress σ_{ij}, or true stress (introduced below), and the infinitesimal strain tensor, ϵ_{ij},

$$\sigma_{ij} = C_{ijkl} \epsilon_{kl} \ , \tag{3.10}$$

where

$$\epsilon_{ij} \doteq \frac{1}{2}(\partial u_i / \partial x_j + \partial u_j / \partial x_i) \ . \tag{3.11}$$

In this special case, the potential energy function can be expressed as

$$W = \frac{1}{2} \epsilon_{ij} C_{ijkl} \epsilon_{kl} \ . \tag{3.12}$$

Since W is a scalar, it follows that $C_{ijkl} = C_{klij}$ (major symmetry) thus reducing the number of independent material constants to 36. Further, the symmetry of the tensors σ_{ij} and ϵ_{ij} require that $C_{ijkl} = C_{jikl}$ and $C_{ijkl} = C_{ijlk}$ (minor symmetry), respectively, thus reducing the number of independent elastic constants to 21 for a fully anisotropic crystal. Depending on the crystal symmetry, the number of independent elastic constants is further reduced: triclinic (13), orthotropic (9), ..., cubic (3). For the special case in which the material has no preferred orientation, an isotropic material, the number of independent elastic constants is 2 (e.g., the bulk and shear moduli, or Young's modulus and Poisson's ratio).

Physically, the energy stored in the material or body is related to the deformations of the atomic and molecular bonds. For nanoscale structures, this fact can be used to define W as a function of the history of $\mathbf{E}$ using the Cauchy–Born

approximation [44, 135, 141, 142]. Interestingly, this approach can also reproduce surface effects [113, 114]. This will be described in more detail in Sect. 3.2.3.

Using Newton's second law, equilibrium of the body $\mathscr{B}$ may be expressed in terms of the divergence of the Cauchy stress tensor in the spatial frame [18],

$$\partial \sigma_{ij}/\partial x_j + b_i = \rho \ddot{u}_i \,, \tag{3.13}$$

where $\ddot{u}_i$ denotes the second derivative of u_i with respect to time, and ρ is the mass density. This set of equilibrium equations can also be cast in terms of other stress tensors, the choice of which is chosen for convenience, using relations such as $\sigma_{ij} = J^{-1} F_{ik} S_{kl} F_{jl}$, where $J = \det(F_{ij})$ [18].

The surface tractions, both normal and shear, are related to the Cauchy stress tensor by the relation

$$t_i = \sigma_{ij} n_j \,, \tag{3.14}$$

where n_j is the unit vector normal to the surface. This relation may be derived using Cauchy's tetrahedron [18], for example.

The field equations of classical continuum mechanics can be solved using a variety of numerical methods including the finite-element method [15, 18] and the boundary-element method [14]. Numerous commercial and research-based nonlinear finite-element solvers are available including Comsol [34], Abaqus [1], and Ansys [6].

3.2.2 Micromorphic Theories

The *micromorphic theories* of Eringen [45, 48, 55, 140] and Mindlin [102] introduce additional microstructural degrees of freedom within a unit cell or "micro-volume." The continuum is now thought of as a continuous collection of deformable cells or particles. *The size of this unit cell introduces a length scale into the continuum theory.* Each cell is free to deform and create a "micro-strain" in addition to the classical macro-strain. The effects of these additional microstructural degrees of freedom include strain-gradient effects, higher-order stresses, surface and size effects, and optical branches of the phonon dispersion curves [26, 27, 56, 102]. Malvern [90] integrates these generalized continuum formulations within his book on continuum mechanics.

Chen et al. [25, 28] give an overview of the hierarchy of generalized continua starting at the most general case with the micromorphic theory of Eringen [45, 48, 140]. With the assumption of infinitesimal linear-elastic deformations, this theory reduces to Mindlin's *microstructure theory* [102]. With the additional assumption that the unit cells are rigid, and thus ignoring internal motion within a cell, the theory reduces to the *micropolar theory* [48]. With the additional assumption that the orientations of the unit cells are fixed, the theory reduces to Cosserat theory [35].

With the additional assumption that the micro-motion is equal to the macro-motion, the theory reduces to the *couple-stress theory* [101, 105, 147, 148]. The classical continuum theory is reproduced when the size of unit cell is reduced to zero or in the long wave-length limit. In general, these formulations can be categorized as "strain-gradient" continuum theories [51, 103, 104, 119]. Various researchers have used these formulations to regularize softening and localization phenomena [92, 93, 150].

In Mindlin's microstructure theory [102], additional deformation modes, called micro-displacements and micro-deformations, are introduced as shown in Fig. 3.1. The macroscopic displacement field is given by $u_i = x_i - X_i$ as usual. A micro-displacement u'_i is defined as $u'_i = x'_i - X'_i$ where X'_i and x'_i are the reference and current positions of a material point within the micro-volume, referred to axes parallel to those of X_i and whose origin moves with displacement u_i (see Fig. 3.1). With the assumption of infinitesimal displacements for both the macro- and micro-displacements, $x_i \approx X_i$ and $x'_i \approx X'_i$. The displacement gradient within the micro-medium is given by

$$\psi_{ij} \doteq \partial u'_j / \partial x'_i \,, \tag{3.15}$$

where ψ_{ij} is called the *micro-deformation*. In Mindlin's theory, ψ_{ij} is taken to be constant within the micro-volume so that

$$u'_j = x'_i \psi_{ij} \,, \tag{3.16}$$

but ψ_{ij} is allowed to vary with position in the macroscale so that $\psi_{ij} = \psi_{ij}(\mathbf{x})$. The macro-gradient of the micro-deformation χ_{ijk} is given by

$$\chi_{ijk} \doteq \partial \psi_{jk} / \partial x_i \,. \tag{3.17}$$

The *relative deformation* γ_{ij} is defined as

$$\gamma_{ij} \doteq \partial u_j / \partial x_i - \partial u'_i / \partial x'_j = \partial u_j / \partial x_i - \psi_{ij} \,. \tag{3.18}$$

The usual infinitesimal strain tensor ϵ_{ij} is defined in Eq. (3.11). Note that while ϵ_{ij} is symmetric, γ_{ij} and χ_{ijk} are not in general symmetric or minor-symmetric, respectively.

The potential energy function per unit macro-volume is posited to be of the form

$$W = W(\epsilon_{ij}, \gamma_{ij}, \chi_{ijk}) \,. \tag{3.19}$$

The following stress tensors[1] are defined to be work conjugate to ϵ_{ij}, γ_{ij}, and χ_{ijk} [102],

[1]Note that the use of the symbols σ and τ is reversed from that of Mindlin [102] to be consistent with our use of σ for the Cauchy stress given in Sect. 3.2.1.

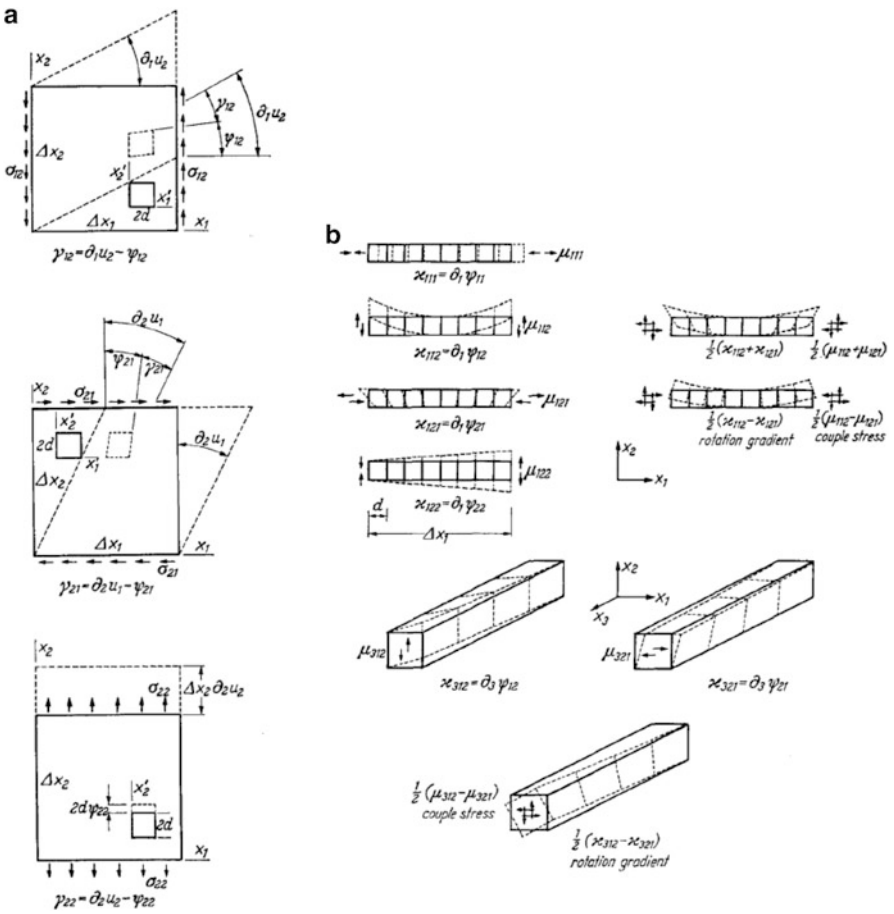

Fig. 3.1 Figures reproduced from Mindlin's original 1964 publication on his *microstructure* (micromorphic) theory [102]. (**a**) Example components of relative stress τ_{ij} (σ_{ij} in Mindlin's notation), displacement gradient $\partial u_i/\partial x_j$, micro-deformation ψ_{ij}, and relative deformation γ_{ij}. (**b**) Example components of the double stress μ_{ijk}, and the gradient of micro-deformation, χ_{ijk} (Reproduced with permission from [102])

$$\sigma_{ij} = \frac{\partial W}{\partial \epsilon_{ij}} \tag{3.20a}$$

$$\tau_{ij} = \frac{\partial W}{\partial \gamma_{ij}} \tag{3.20b}$$

$$\mu_{ijk} = \frac{\partial W}{\partial \chi_{ijk}} \,, \tag{3.20c}$$

where σ_{ij} is interpreted as the Cauchy stress tensor, τ_{ij} is the *relative stress* tensor, and μ_{ijk} is the *double stress* tensor. The twenty-seven components of μ_{ijk} represent *double-forces* per unit area. Example components of μ_{ijk} are shown in Fig. 3.1. Note that while σ_{ij} is symmetric, τ_{ij} and μ_{ijk} are not in general symmetric or minor-symmetric, respectively.

Developing expressions for the kinetic energy and using Hamilton's principle results in the following twelve equations of motion [102]:

$$\partial(\sigma_{ij} + \tau_{ij})/\partial x_i + b_j = \rho \ddot{u}_j \tag{3.21a}$$

$$\mu_{ijk,i} + \tau_{jk} + \Phi_{jk} = \frac{1}{3}\rho' d_{lj}^2 \ddot{\psi}_{lk} \ , \tag{3.21b}$$

with twelve traction boundary conditions,

$$t_j = (\sigma_{ij} + \tau_{ij})\, n_i \tag{3.22a}$$

$$T_{jk} = \mu_{ijk}\, n_i \ . \tag{3.22b}$$

Here, ρ' is the mass of the micro-material per unit macro-volume, d_{lk} is a unit-cell moment-of-inertia tensor, Φ_{jk} is a double-force per unit volume, and T_{jk} is a double-force per unit area [102].

Similar to the expression for W for the classical continuum formulation, Eq. (3.12), the potential energy of a microstructural continuum is taken to be a quadratic function of the forty-two variables ϵ_{ij}, γ_{ij}, and χ_{ijk},

$$W = \frac{1}{2}\epsilon_{ij} C_{ijkl} \epsilon_{kl} + \frac{1}{2}\gamma_{ij} B_{ijkl} \gamma_{kl} + \frac{1}{2}\chi_{ijk} A_{ijklmn} \chi_{lmn} \tag{3.23a}$$

$$+ \gamma_{ij} D_{ijklm} X_{klm} + \chi_{ijk} F_{ijklm} \epsilon_{lm} + \gamma_{ij} G_{ijkl} \epsilon_{kl} \ . \tag{3.23b}$$

The constitutive equations are then,

$$\sigma_{ij} = C_{ijpq}\epsilon_{pq} + G_{pqij}\gamma_{pq} + F_{pqrij}\chi_{pqr} \tag{3.24a}$$

$$\tau_{ij} = G_{ijpq}\epsilon_{pq} + B_{pqij}\gamma_{pq} + D_{ijpqr}\chi_{pqr} \tag{3.24b}$$

$$\mu_{ijk} = F_{ijkpq}\epsilon_{pq} + D_{pqijk}\gamma_{pq} + A_{ijkpqr}\chi_{pqr} \ . \tag{3.24c}$$

As noted by Mindlin [102], only 903 of these 1764 coefficients are independent due to the symmetry of ϵ_{ij} and the scalar property of W. Still, this number is vastly larger than 21 independent elastic constants for a fully anisotropic classical linear-elastic continuum described in Sect. 3.2.1. Even for an idealized isotropic microstructural medium, there are 18 independent coefficients [102].

A general three-dimensional finite-element implementation of the micromorphic continuum theory is ongoing within the Tahoe Development Project [143].

3.2.3 Surface Stress

For nanoscale structures, surface-to-volume ratios are relatively large, and surface effects can become significant [23, 40, 59, 134, 152]. Surface effects, including edge and vertex effects, arise in atomic systems fundamentally due to the difference in the coordination number of atoms near the surface versus atoms in the interior and due to long-range atomic forces beyond nearest-neighbor interactions. These in turn lead to differences in the charge distributions, bond lengths, and bond angles near the surface versus the interior [67].

Gurtin et al. [57–59] have developed a general continuum theory for elastic material surfaces and material interfaces. For solids, the concepts of surface tension, surface stress, and surface energy are distinctly different and cannot be used interchangeably. Only for liquids are all three the same [67]. (Chap. 17 of this book discusses surface-tension effects in thin liquid films.) For the special case of small deformations, these three quantities are related via the equation[2] [67],

$$\boldsymbol{\sigma}^{\mathrm{s}} = \sigma\, \mathbf{I}^{\mathrm{s}} + \frac{\partial \Gamma}{\partial \boldsymbol{\epsilon}^{\mathrm{s}}} \,, \tag{3.25}$$

where $\boldsymbol{\sigma}^{\mathrm{s}}$ is the surface-stress tensor, σ is the surface tension, $\mathbf{I}^{\mathrm{s}}$ is the identity tensor for surfaces, $\Gamma(\boldsymbol{\epsilon}^{\mathrm{s}})$ is the deformation-dependent surface energy, and $\boldsymbol{\epsilon}^{\mathrm{s}}$ is surface-strain tensor. Each tensor in this equation is defined in the surface manifold and has 2×2 components. For the idealized case of an isotropic material (surface and bulk) the following equilibrium and constitutive equations hold. For the bulk material, the equilibrium equations are the same as those given in Sect. 3.2.1, Eq. (3.13), but with the constitutive equations, Eq. (3.10), specialized for an isotropic material,

$$\operatorname{div} \boldsymbol{\sigma}^{\mathrm{b}} = 0 \tag{3.26a}$$

$$\boldsymbol{\sigma}^{\mathrm{b}} = 2\mu \boldsymbol{\epsilon}^{\mathrm{b}} + \lambda \operatorname{Tr}(\boldsymbol{\epsilon}^{\mathrm{b}})\, \mathbf{I}^{\mathrm{b}} \,, \tag{3.26b}$$

where $\boldsymbol{\sigma}^{\mathrm{b}}$ is the Cauchy stress in the bulk material, $\boldsymbol{\epsilon}^{\mathrm{b}}$ is the infinitesimal strain tensor in the bulk, $\operatorname{div}(\cdot)$ is the bulk divergence operator, λ and μ are the Lame' constants, $\operatorname{Tr}(\cdot)$ is the trace operator, and $\mathbf{I}^{\mathrm{b}}$ is the three-dimensional identity tensor. Equilibrium of the surface of the material, or interface between two materials, is given by [59, 134],

$$0 = [\boldsymbol{\sigma}^{\mathrm{b}} \cdot \mathbf{n}] + \operatorname{div}_{\mathrm{s}} \boldsymbol{\sigma}^{\mathrm{s}} \tag{3.27a}$$

$$\boldsymbol{\sigma}^{\mathrm{s}} = \sigma\, \mathbf{I}^{\mathrm{s}} + 2(\mu^{\mathrm{s}} - \sigma)\boldsymbol{\epsilon}^{\mathrm{s}} + (\lambda^{\mathrm{s}} + \sigma) \operatorname{Tr}(\boldsymbol{\epsilon}^{\mathrm{s}})\, \mathbf{I}^{\mathrm{s}} \,, \tag{3.27b}$$

[2] In this section, we use vector notation to simplify the representation of surface tensors.

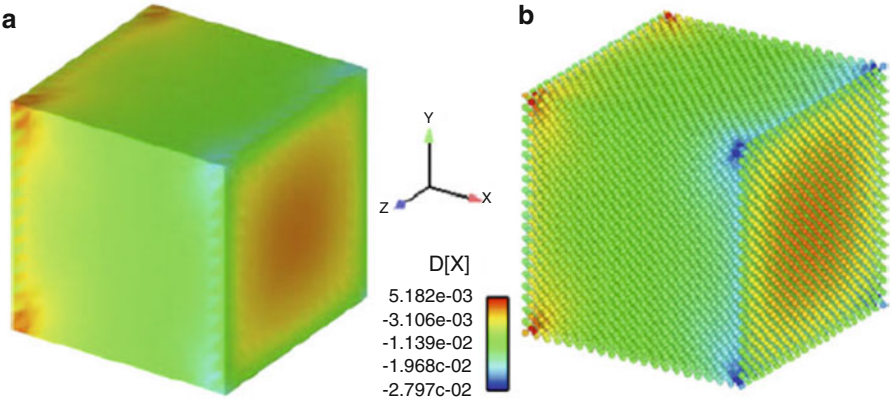

Fig. 3.2 The x-component of the displacement vector after the relaxation of a cube as calculated by (**a**) surface Cauchy–Born method and (**b**) molecular statics simulation (Reproduced with permission from [114])

where $\mathrm{div}_s(\cdot)$ is the surface divergence operator, λ^s and μ^s are the surface Lamé constants, and the square brackets in Eq. (3.27a) represent the jump in the quantity across the interface.

Determining the surface material constants in this continuum formulation is nontrivial [59, 67, 100] and somewhat ill-defined. (For example, how thick is the surface or interface?) At the nanoscale, when the surface effects are most prominent, the surface material constants are expected to depend on the orientation of the surface with respect to the underlying crystal lattice. Determining the material constants for all possible orientations of a surface is a daunting prospect. For these reasons, computational approaches based on the Cauchy–Born approximation have been pursued to model surface effects [113, 114]. In this approach, the surface and bulk strain energies are calculated directly using interatomic potentials, and the constitutive response is obtained using Eq. (3.7). The continuum displacement field is obtained by minimizing the total potential energy. An example from Park et al. [114] is shown in Fig. 3.2. This approach has the further advantage of incorporating edge and vertex effects that depend on the included angle of the intersecting surfaces and edges, respectively. This "quasi-continuum" approach to modeling nanoscale structures is described in detail in Chap. 5 of this book.

3.2.4 Nonlocal Theories

Nonlocal continuum theories were introduced by Kröner [78] in order to account for the long-range interactions present in atomic systems. These theories were later studied and further developed by Eringen [46, 47]. The relations between nonlocal

theories and strain-gradient theories have been studied by several authors [2, 3, 120, 123, 124]. Nonlocal theories have been used to model nanoscale structures [7, 118, 151], and have been applied to macroscale systems in order to regularize strain-softening behavior [69, 120]. In Eringen's nonlocal theory, the nonlocal stress tensor $\boldsymbol{\sigma}(\mathbf{x})$ is related to the local (fictitious) stress tensor $\mathbf{s}(\mathbf{x})$ through an integral relation of the form

$$\boldsymbol{\sigma}(\mathbf{x}) = \int_V A(\mathbf{x}, \mathbf{x}')\mathbf{s}(\mathbf{x}')\, dV' \,, \tag{3.28}$$

where $A(\mathbf{x}, \mathbf{x}')$ is a scalar valued *attenuation function* or influence function, and $\mathbf{s}(\mathbf{x})$ is related to the local strain via the classical relation given by Eq. (3.10), $\mathbf{s}(\mathbf{x}) = \mathbb{C} : \boldsymbol{\epsilon}(\mathbf{x})$. The attenuation function is typically defined to be nonzero only within a certain radius R of the given point $\mathbf{x}$ so that $A(\mathbf{x}, \mathbf{x}') = 0$ when $||\mathbf{x}' - \mathbf{x}|| > R$. The attenuation function must be modified near the boundary of the domain to ensure certain consistency requirements in representing constant fields. This boundary effect in nonlocal models may be physically desired depending on the physical system being modeled.

An alternate nonlocal continuum formulation, called *peridynamics*, has been proposed by Silling [136–138]. In this formulation, the concept of strain is avoided all together in favor of generalized *bonds* connecting two disconnected points within a domain.

$$\int_V \mathbf{f}(\mathbf{u}' - \mathbf{u}, \mathbf{x}' - \mathbf{x})\, dV' + \mathbf{b} = \rho\ddot{\mathbf{u}} \,, \tag{3.29}$$

where $\mathbf{u}$ is the displacement vector, ρ is the mass density, $\mathbf{b}$ is the body force per unit volume, and $\mathbf{f}$ represents the *force density* per unit volume. This *bond-based* formulation has been generalized to the so-called *state-based* formulation [138] that allows for very general material behavior. Applications of peridynamics to the upscaling of molecular dynamics have been studied by Seleson et al. [125] with recent applications to nanomechanics [17, 42]. The peridynamic theory now has been extensively developed [49, 137]. Peridynamics has been implemented in the open-source massively parallel software LAMMPS [80, 115, 116].

3.3 Homogenization Theory

Homogenization is the mathematical process of replacing a heterogeneous material with a fictitious homogeneous material whose macroscopic response, in an energetic sense, is equal to that of the true heterogeneous material. The material properties of the fictitious homogeneous material are called the *effective* properties [65]. Homogenization is fundamental to continuum mechanics, since all materials are heterogeneous or discrete at some length scale and require homogenization in

order to apply continuum principles at a higher length scale. There are several texts that cover homogenization theory for various physics and to various levels of mathematical rigor [16, 30, 50, 68, 95, 110, 117, 133]. The theory is well developed for materials with periodic microstructure using perturbation theory and the mathematical concepts of strong and weak convergence. The theory has been extended to random microstructures by Papanicolaou and Varadhan [112] using probabilistic definitions of convergence. Section 3.3.1 gives an overview of the two-scale asymptotic homogenization process for linear-elastic periodic microstructures. This mathematical approach is well developed, and leads to the concepts of higher-order stresses or "hyperstresses." Section 3.3.2 discusses the mathematical concepts of strong and weak convergence. Section 3.3.3 presents a three-dimensional homogenization example. The homogenization results of this example are compared to direct numerical simulations (DNS) of the heterogeneous microstructure. Section 3.3.4 discusses the concept of computational homogenization. Additionally, Sect. 3.3.4 discusses the fast Fourier transform (FFT) method for efficiently solving the unit-cell problem, in both the linear and nonlinear regimes.

Mean-field homogenization techniques such as the self-consistent method [106] do not attempt to directly model the exact field of a heterogeneous microstructure, but instead focus on modeling the response of a single inclusion within an approximately homogeneous continuum. Mean-field methods are not discussed here, but are covered in detail by Nemat-Nasser and Hori [110] along with other topics in the theory of composite materials.

3.3.1 Method of Two-Scale Asymptotic Expansion

Tran et al. [149] give a succinct yet detailed presentation of the two-scale asymptotic homogenization process for linear-elastic periodic microstructures. Their notation and presentation is followed here. Let L represent the length scale of the macrostructure. Let l represent the length scale of the unit cell. The ratio $\epsilon \doteq l/L$ of the two length scales is assumed to be less than 1, but not necessarily infinitesimally small. The existence of the small parameter ϵ suggests the use of perturbation theory [63]. A new "fast" oscillating variable is introduced as $\mathbf{y} \doteq \mathbf{x}/l$ which gives the position within an individual cell. The displacement field is now considered as a function of the two variables $\mathbf{x}$ and $\mathbf{y}$ so that $\mathbf{u} = \mathbf{u}(\mathbf{x}, \mathbf{y})$. The displacement field is expanded in a power series in ϵ,

$$\mathbf{u}(\mathbf{x}, \mathbf{y}) = \mathbf{u}^0(\mathbf{x}, \mathbf{y}) + \epsilon \mathbf{u}^1(\mathbf{x}, \mathbf{y}) + \epsilon^2 \mathbf{u}^2(\mathbf{x}, \mathbf{y}) + \cdots , \tag{3.30}$$

where the fields $\mathbf{u}^i(\mathbf{x}, \mathbf{y})$, $i = 1, 2, 3, \ldots$ are periodic with period l. This expansion is then substituted into Eqs. (3.10) and (3.13). By equating terms with the same power of ϵ, a hierarchy of cell problems for the quantities $\mathbf{u}^0(\mathbf{x}, \mathbf{y})$, $\mathbf{u}^1(\mathbf{x}, \mathbf{y})$, $\mathbf{u}^2(\mathbf{x}, \mathbf{y})$, etc., is obtained. It transpires that $\mathbf{u}^0(\mathbf{x}, \mathbf{y})$ is only a function of $\mathbf{x}$. With

$\mathbf{u}^0(\mathbf{x},\mathbf{y}) \doteq \mathbf{U}(\mathbf{x})$, it can be shown that $\mathbf{U}(\mathbf{x}) = \frac{1}{V}\int_V \mathbf{u}(\mathbf{x},\mathbf{y})\,dV$ where V is the volume of a unit cell. $\mathbf{U}(\mathbf{x})$ is then interpreted as the displacement of the centroid of the unit cell [149].

The total displacement field $\mathbf{u}(\mathbf{x},\mathbf{y})$ can now be written as

$$\mathbf{u}(\mathbf{x},\mathbf{y}) = \mathbf{U}(\mathbf{x}) + \epsilon\boldsymbol{\chi}^1(\mathbf{y}) : \mathbf{E}(\mathbf{x}) + \epsilon^2\boldsymbol{\chi}^2(\mathbf{y}) : \cdot\,\mathbf{G}(\mathbf{x}) + \cdots\,, \tag{3.31}$$

where $\boldsymbol{\chi}^i(\mathbf{y})\,, i = 1, 2, 3, \ldots$ are called localization tensors and are obtained through the solution of the hierarchy of cell problems [149]. Here, $\mathbf{E}(\mathbf{x})$ is interpreted as the macroscopic strain tensor with

$$\mathbf{E}(\mathbf{x}) = \int_V \epsilon(\mathbf{x},\mathbf{y})\,dV\,, \tag{3.32}$$

and $\mathbf{G}(\mathbf{x})$ is interpreted as the non-dimensional gradient of macroscopic strain, $\mathbf{G}(\mathbf{x}) = L\,\nabla\mathbf{E}(\mathbf{x})$. The additional terms in Eq. (3.31) consist of products of higher-order strain-gradients and localization tensors.

Tran et al. [149] were able to derive a generalization of the classical Hill–Mandel lemma,

$$\frac{1}{V}\int_V \boldsymbol{\sigma}(\mathbf{x},\mathbf{y}) : \boldsymbol{\epsilon}(\mathbf{x},\mathbf{y})\,dV = \boldsymbol{\Sigma}(\mathbf{x}) : \mathbf{E}(\mathbf{x}) + \mathbf{T}(\mathbf{x}) : \cdot\,\nabla\mathbf{E}(\mathbf{x}) + \cdots\,, \tag{3.33}$$

where $\boldsymbol{\Sigma}(\mathbf{x})$ is interpreted as the macroscopic stress, and $\mathbf{T}(\mathbf{x})$ is the "first hyper-stress." The additional terms in Eq. (3.33) consist of products of hyperstresses and higher-order strain gradients. It can be shown that

$$\frac{1}{V}\int_V \sigma_{ij}(\mathbf{x},\mathbf{y})\,dV = \Sigma_{ij}(\mathbf{x}) - T_{ijk,k}(\mathbf{x}) + \cdots\,. \tag{3.34}$$

The macroscopic balance equation is given by [149]

$$\Sigma_{ij,j}(\mathbf{x}) - T_{ijk,jk}(\mathbf{x}) + \cdots + B_i = 0, \tag{3.35}$$

where $B_i = \frac{1}{V}\int_V b_i(\mathbf{x},\mathbf{y})\,dV$ is the cell-averaged body force.

In the limit as $\epsilon \to 0$ or negligible strain gradients, $\nabla\mathbf{E}(\mathbf{x}) \to 0$, the hyperstresses are zero, and the classical homogenization results are recovered,

$$\frac{1}{V}\int_V \boldsymbol{\sigma}(\mathbf{x},\mathbf{y}) : \boldsymbol{\epsilon}(\mathbf{x},\mathbf{y})\,dV = \boldsymbol{\Sigma}(\mathbf{x}) : \mathbf{E}(\mathbf{x}), \tag{3.36a}$$

$$\frac{1}{V}\int_V \sigma_{ij}(\mathbf{x},\mathbf{y})\,dV = \Sigma_{ij}(\mathbf{x}), \tag{3.36b}$$

$$\Sigma_{ij,j}(\mathbf{x}) + B_i = 0\,. \tag{3.36c}$$

The homogenized material properties relating the macroscopic stress Σ_{ij} to macroscopic strain E_{ij}, as well as relating the hyperstresses to the strain gradients (e.g., T_{ijk} to $E_{ij,k}$), are obtained from the unit-cell problems described previously. These are described by Tran et al. [149]. For first-order homogenization theory ($\epsilon \to 0$), the cell problem is given by

$$\sigma_{ij,j}(\mathbf{y}) = 0, \tag{3.37a}$$

$$\sigma_{ij}(\mathbf{y}) = C_{ijkl}(\mathbf{y})\epsilon_{kl}(\mathbf{y}) + p_{ij}(\mathbf{y}), \tag{3.37b}$$

$$\epsilon_{kl}(\mathbf{y}) = \frac{1}{2}\left(\partial u_k(\mathbf{y})/\partial y_l + \partial u_l(\mathbf{y})/\partial y_k\right), \tag{3.37c}$$

$$u_i(\mathbf{y}) \text{ periodic}, \quad \frac{1}{V}\int_V u_i(\mathbf{y})\, dV = 0. \tag{3.37d}$$

where $p_{ij}(\mathbf{y})$ is a polarization tensor given by $p_{ij}(\mathbf{y}) = C_{ijkl}(\mathbf{y})E_{kl}$, and E_{kl} is constant over the unit cell. By applying unit values of E_{kl} for each of the components, the homogenized stiffness tensor can be obtained. More complex polarization tensors and body forces arise for the higher-order cell problems. Because of the periodic boundary conditions, an efficient solution of this unit-cell problem can be obtained through the use of the FFT as described in Sect. 3.3.4. These results can be extended to the nonlinear regime using "computational homogenization" as described in Sect. 3.3.4.

As with atomic systems, the confinement of the unit cell at the surface of a body is different than a unit cell that is positioned within the bulk. In particular, at the surface the unit cell does not experience periodic boundary conditions. Thus, a surface effect will result when comparing unit-cell averages obtained from homogenization and unit-cell averages obtained from direct numerical calculations of the full heterogeneous material. This will be demonstrated in the example presented in Sect. 3.3.3.

3.3.2 Convergence: Strong and Weak

One of the main mathematical results of homogenization theory is that in the limit as $\epsilon \to 0$ the displacement solution of the macroscopic governing field equation containing the heterogeneous material converges *strongly* to the displacement solution of the macroscopic field equation containing the homogenized material [30]. Furthermore, in the limit as $\epsilon \to 0$ the strain (stress) field of the macroscopic field equation containing the heterogeneous material converges *weakly* to the strain (stress) field of the macroscopic field equation containing the homogenized material [30].

Recall that a sequence of functions (u_n), $n = 1, 2, 3, \ldots$, with $u_n \in L^2$, converges *strongly* to $u \in L^2$ if

$$\lim_{n\to\infty} \|u_n - u\| = 0\,, \tag{3.38}$$

and converges *weakly* if

$$\lim_{n\to\infty} \langle u_n, v\rangle = \langle u, v\rangle \quad \forall v \in L^2\,. \tag{3.39}$$

Here L^2 represents the space of square-integrable functions, $\langle u, v\rangle$ represents the L^2 inner product, and $\|u\| = \sqrt{\langle u, u\rangle}$ is the norm induced by the inner product.

For an example illustrating strong and weak convergence, consider a one-dimensional continuous bar of length L with variable elastic modulus, $E(x)$, given by

$$E(x) = E_0(1 + a\sin(2n\pi x/L)) \quad x \in [0, L] \quad n = 1, 2, 3, \tag{3.40}$$

where $a \in [0, 1)$ is a parameter that governs the degree of inhomogeneity. For this problem, the spatial period or unit cell is $l = L/n$ (*cf.* example problems given in the Appendix). For a one-dimensional bar, the governing equations given in Sect. 3.2.1 reduce to the following ordinary differential equation:

$$\frac{d}{dx}\left(E(x)\frac{du}{dx}\right) = 0, \tag{3.41}$$

where $u = u(x)$ is the uniaxial displacement along the bar. This equation may be integrated analytically using displacement boundary conditions $u(0) = 0$ and $u(L) = u_0$ to give the exact displacement field,

$$u(x) = \frac{u_0}{n\pi}\left[\pi\,\lfloor nx/L + 1/2\rfloor + \tan^{-1}\left(\frac{\tan\left(\frac{n\pi x}{L}\right) + a}{\sqrt{1-a^2}}\right) - \tan^{-1}\left(\frac{a}{\sqrt{1-a^2}}\right)\right] \tag{3.42}$$

with derivative (longitudinal strain) given by

$$\frac{du}{dx} = \frac{u_0}{L}\frac{\sqrt{1-a^2}}{1 + a\sin(2n\pi x/L)}\,. \tag{3.43}$$

In Eq. (3.42), the function $\lfloor\cdot\rfloor$ is the floor function, and the inverse tangent functions are understood to give principal values. These functions are plotted in Fig. 3.3 for $a = 0.9$ and $n = 5, 10, 20$. The displacement field of the homogenized beam, $u^0(x)$, is given simply by

$$u^0(x) = u_0\frac{x}{L}\,, \tag{3.44}$$

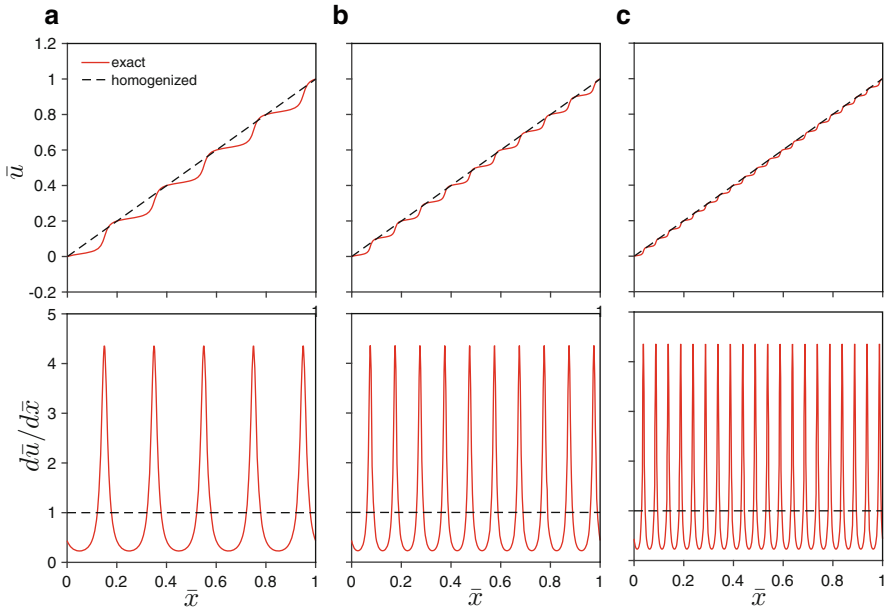

Fig. 3.3 Example of both strong (*top row*) and weak convergence (*bottom row*) using a one-dimensional continuous bar of length L with periodic elastic modulus given by Eq. (3.40). The exact displacement field is given by Eq. (3.42), and is shown here for the cases (**a**) $n = 5$, (**b**) $n = 10$, (**c**) $n = 20$ (*top row*), with $a = 0.9$ and $\bar{u} \doteq u/u_0$, $\bar{x} \doteq x/L$. This displacement converges *strongly* to the displacement field $\bar{u}(x) = \bar{x}$ as $n \to \infty$. However, the exact displacement derivative (strain), given by Eq. (3.43), converges only *weakly* to the derivative of the homogenized solution $d\bar{u}/d\bar{x} = 1$ as $n \to \infty$ (*bottom row*)

with constant derivative

$$\frac{du^0}{dx} = \frac{u_0}{L} \,. \tag{3.45}$$

These functions are also plotted in Fig. 3.3. It can be proven that $u(x)$ converges *strongly* to u^0 as $n \to \infty$, which is clear via inspection of Fig. 3.3. What is less clear, but still true, is that du/dx converges *weakly* to du^0/dx as $n \to \infty$.

It is instructive to verify the equivalency of the total energy stored using the two descriptions of the bar, direct and homogenized. For this one-dimensional example, the energy density given by Eq. (3.12) reduces to

$$W = \frac{1}{2} E(x) \left(\frac{du}{dx} \right)^2 \,, \tag{3.46}$$

where $E(x)$ is given by Eq. (3.40) and du/dx is given by Eq. (3.43). The total stored energy in the bar W_{total} is then

$$W_{\text{total}} = \int_0^L W\,dx = \frac{1}{2}E_0(1-a^2)\left(\frac{u_0}{L}\right)^2 \int_0^L \frac{1}{1+a\sin(2n\pi x/L)}dx$$
$$= \frac{1}{2}E_0\sqrt{1-a^2}\left(\frac{u_0}{L}\right)^2 L\,. \tag{3.47a}$$

For the homogenized bar, the effective modulus E^0 is simply the harmonic mean of the modulus within the unit cell[3] [30],

$$\frac{1}{E^0} = \frac{1}{l}\int_0^l \frac{1}{E(x)}dx = \frac{1}{l}\int_0^l \frac{1}{E_0(1+a\sin(2\pi x/l))}dx$$
$$= \frac{1}{E_0}\frac{1}{2\pi}\int_0^{2\pi} \frac{1}{1+a\sin(\xi)}d\xi = \frac{1}{E_0}\frac{1}{\sqrt{1-a^2}}\,. \tag{3.48a}$$

Thus,

$$E^0 = E_0\sqrt{1-a^2}\,. \tag{3.49}$$

The energy density of the homogenized bar W^0 is given by

$$W^0 = \frac{1}{2}E^0\left(\frac{du^0}{dx}\right)^2\,, \tag{3.50}$$

where E^0 is given by Eq. (3.49) and du^0/dx is given by Eq. (3.45). The total stored energy in the homogenized bar W^0_{total} is then

$$W^0_{\text{total}} = \int_0^L W^0\,dx = W^0 L = \frac{1}{2}E_0\sqrt{1-a^2}\left(\frac{u_0}{L}\right)^2 L\,, \tag{3.51}$$

which is identical to W_{total} given by Eq. (3.47a), as required.

3.3.3 Homogenization Example

For a homogenization example, consider the unit cell shown in Fig. 3.4a. This unit cell is a cube partitioned into nine subvolumes. In the center of the unit cell is a truncated octahedron. The remaining eight parts are the corners of the cube not contained in the truncated octahedron. We take each subvolume of the cube to be a crystal of stainless steel 304L (γ-Fe). The FCC crystal structure of γ-Fe (austenite) possesses cubic elastic symmetry with a relatively large anisotropy ratio A, with

[3] This simple relation does not hold in higher-dimensional problems.

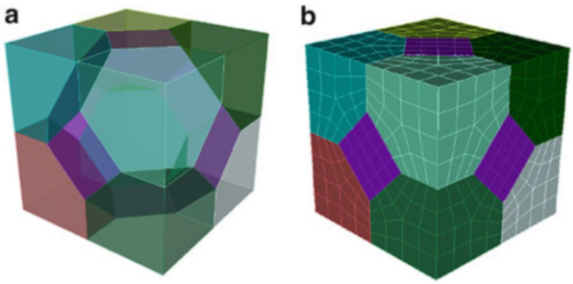

Fig. 3.4 (**a**) Example unit cell consisting of nine subvolumes. The center subvolume is a truncated octahedron. (**b**) Conformal hexahedral finite-element mesh of the unit cell

Table 3.1 Cubic elasticity constants for 304L stainless steel (γ-Fe) [81] (units are GPa)

Material	C_{11}	C_{12}	C_{44}	A
304L	204.6	137.7	126.2	3.8
α-Fe	231.4	134.7	116.4	2.4
Al	107.3	60.9	28.3	1.2
Cu	168.4	121.4	75.4	3.2

The anisotropy ratio $A = 2C_{44}/(C_{11} - C_{12})$ is also given. For an isotropic material, $A = 1$. Several other cubic metals are given for comparison [19]

$A \doteq 2C_{44}/(C_{11} - C_{12}) = 3.8$, where C_{11}, C_{12}, and C_{44} are the cubic elastic constants. For an isotropic material, $A = 1$. The values of these constants are given in Table 3.1 for austenite [81] along with several other cubic materials for comparison [19]. The relatively large anisotropy ratio of austenite should produce more pronounced surface and strain-gradient effects within a macroscale structure containing finite microstructure.

The orientation of each crystal (subvolume) within the unit cell is chosen such that the homogenized (first-order) material properties of the unit cell are orthotropic. For the truncated octahedron subvolume, the crystal aligns with the axes of the unit cell. For each corner subvolume, one axis of the crystal is in a $\langle 111 \rangle$ direction. The second axis is in a $\langle 110 \rangle$ direction.

The homogenized elastic constants (first-order) are obtained by solving the boundary-value problem defined in Eq. (3.37). The polyhedral algorithm within the Cubit meshing tool [36] was used to create a hexahedral mesh of each subvolume as shown in Fig. 3.4b. The finite-element mesh of the unit cell contained 832 hexahedral elements. Results were insensitive to further mesh refinement. The homogenized material properties are $E_1 = E_2 = 1.15737 \times 10^5$, $E_3 = 0.980940 \times 10^5$, $\mu_{12} = 5.01817 \times 10^4$, $\mu_{13} = \mu_{23} = 5.89234 \times 10^4$, $\nu_{21} = 0.26924$, $\nu_{31} = \nu_{32} = 0.38072$, where E_i, μ_i, ν_{ij}, $i, j = 1, 2, 3$ are the orthotropic Young's moduli, shear moduli, and Poisson's ratios, respectively. Note there is some additional symmetry present, since there are only six independent elastic constants whereas a fully orthotropic material has nine independent elastic constants. Additionally, recall that for an orthotropic material, $\nu_{12} = \frac{E_1}{E_2}\nu_{21}$, $\nu_{13} = \frac{E_1}{E_3}\nu_{31}$, and $\nu_{23} = \frac{E_2}{E_3}\nu_{32}$.

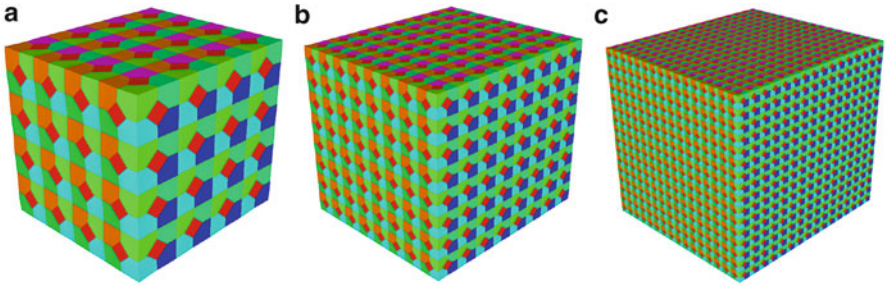

Fig. 3.5 Aggregates of the unit cell shown in Fig. 3.4: (**a**) $4 \times 4 \times 4$, (**b**) $8 \times 8 \times 8$, (**c**) $16 \times 16 \times 16$ (The color of each subvolume with the unit cell is arbitrary)

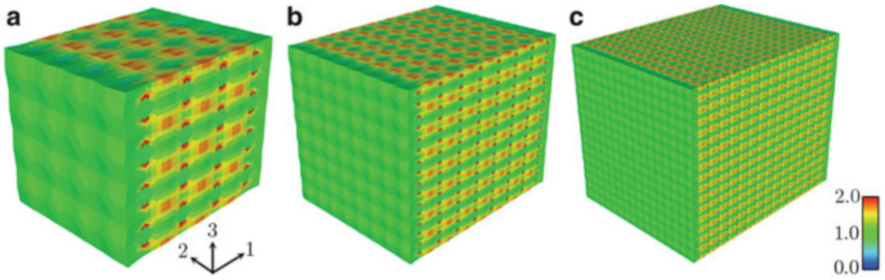

Fig. 3.6 Stress component σ_{11} resulting from the application of a uniform unit traction on the two surfaces normal to the [100] direction of the crystal structures shown in Fig. 3.5. (**a**) $4 \times 4 \times 4$, (**b**) $8 \times 8 \times 8$, (**c**) $16 \times 16 \times 16$. Note the apparent surface effects near the two planes on which the tractions are applied. For this simple loading case, the stress field resulting from the use of the homogenized material properties is $\sigma_{11} = 1$ with all other components identically zero. On the interior, the stress field is approximately periodic

Note that $E_1/E_3 = 1.17986$. Thus, the unit cell exhibits a significantly smaller (homogenized) anisotropy than the individual cubic crystals.

Now consider the $4 \times 4 \times 4$, $8 \times 8 \times 8$, and $16 \times 16 \times 16$ aggregates of unit cells as shown in Fig. 3.5. A uniform traction of unit value is applied to the two surfaces normal to the [100] direction. The resulting stress field is shown in Fig. 3.6 (component σ_{11}). For this simple loading case, the stress field resulting from the use of the homogenized material properties is $\sigma_{11} = 1$ with all other components identically zero. Note the apparent surface effects near the two planes on which the tractions are applied. Also, the surface effect does not disappear as the size of the unit cell gets smaller relative to the overall aggregate size. The stress field at the surface consistently deviates from that of the interior. In the interior, the stress field is approximately periodic.

In order to introduce macroscale strain gradients, consider the boundary-value problem of a linear-elastic prismatic beam of length L and rectangular cross-section of width $2a$ and height $2b$ as shown in Fig. 3.7a. The beam is fixed (weakly) on the end $x_3 = L$, and subjected to a transverse shear force F in the negative x_2-direction

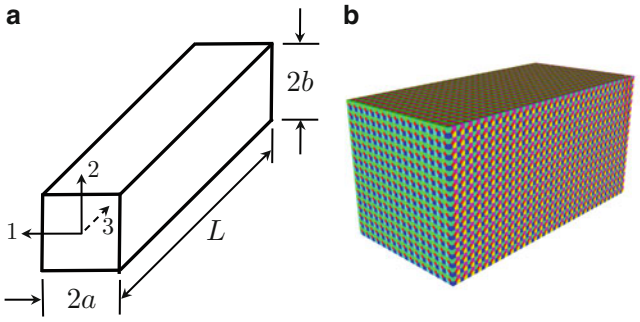

Fig. 3.7 (**a**) Prismatic beam of length L and rectangular cross-section of width $2a$ and height $2b$. (**b**) Beam consisting of $16 \times 16 \times 32$ unit cells shown in Fig. 3.4. For this case, $2a = 2b = 1$, $L = 2$

at the opposite end $x_3 = 0$. At any cross-section of the beam

$$\int_{-b}^{b}\int_{-a}^{a} \sigma_{32}\, dx_1\, dx_2 = F \quad \text{and} \quad \int_{-b}^{b}\int_{-a}^{a} \sigma_{33} x_2\, dx_1\, dx_2 = F x_3\,, \tag{3.52}$$

so that the beam transmits a constant shear force on each cross-section, and the bending moment about the x_1-axis increases linearly from zero at $x_3 = 0$ to FL at $x_3 = L$. The transverse faces are traction free. For an isotropic material, Barber [12] gives the exact Cauchy stress field as

$$\sigma_{11} = \sigma_{21} = \sigma_{22} = 0 \tag{3.53a}$$

$$\sigma_{33} = \frac{F}{I} x_2 x_3 \tag{3.53b}$$

$$\sigma_{31} = \frac{F}{I}\frac{2a^2}{\pi^2}\frac{\nu}{1+\nu}\sum_{n=1}^{\infty}\frac{(-1)^n}{n^2}\sin(n\pi x_1/a)\frac{\sinh(n\pi x_2/a)}{\cosh(n\pi b/a)} \tag{3.53c}$$

$$\sigma_{32} = \frac{F}{I}\frac{b^2 - x_2^2}{2} + \frac{F}{I}\frac{\nu}{1+\nu}\left[\frac{3x_1^2 - a^2}{6} - \frac{2a^2}{\pi^2}\sum_{n=1}^{\infty}\frac{(-1)^n}{n^2}\cos(n\pi x_1/a)\frac{\cosh(n\pi x_2/a)}{\cosh(n\pi b/a)}\right] \tag{3.53d}$$

where ν is Poisson's ratio, and $I = 4ab^3/3$ is the second moment-of-area about the x_1-axis. An analysis of the derivation of this stress field shows that the solution also holds for the special case of an orthotropic material with the additional symmetries $E_1 = E_2$, $\mu_{13} = \mu_{23}$, and $\nu_{31} = \nu_{32}$. This is precisely the case for the unit cell considered in this example. The only modification required of Eq. (3.53) is to let $\nu \to \nu_{31} = \nu_{32}$.

Figure 3.7 shows a beam consisting of $16 \times 16 \times 32$ unit cells. For this case, $2a = 2b = 1$, $L = 2$, and $l/L = 1/16$. The total size of the finite-element mesh

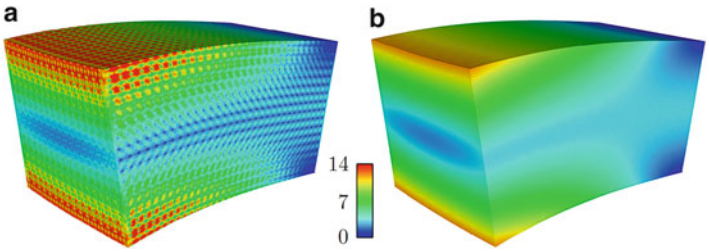

Fig. 3.8 (**a**) Von Mises stress field of the heterogeneous beam shown in Fig. 3.7. The beam is fixed (weakly) on the end $x_3 = L$, and subjected to a transverse shear force in the negative x_2-direction at the opposite end $x_3 = 0$. (**b**) Von Mises stress field of the same beam but instead using the homogenized material properties (The deformed shape is shown greatly magnified)

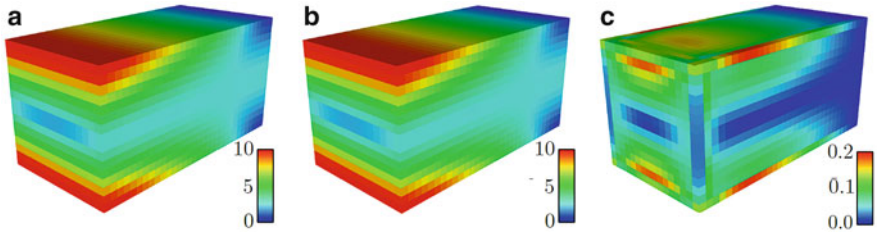

Fig. 3.9 (**a**) Magnitude of the cell-averaged Cauchy stress tensor for the heterogeneous beam. (**b**) Magnitude of the cell-averaged Cauchy stress tensor for the homogeneous beam. (**c**) Magnitude of the difference in the cell-averaged Cauchy stress tensors

is then $832 \times 8192 \approx 6.8$ million. Tractions are applied on the surfaces $x_3 = 0$ and $x_3 = L$ according to Eq. (3.53). The resulting Von Mises stress field is shown in Fig. 3.8a. The Von Mises stress field of the same beam, but instead using the homogenized unit-cell material properties, is shown in Fig. 3.8b.

To investigate the accuracy of homogenization solution for this example, we consider the average of the stress tensor over the unit cell according to Eq. (3.34) for both the DNS results and the homogenization results (H). Any difference can be attributed to either surface effects or hyperstresses. Figure 3.9a, b gives the Euclidean magnitude $||\langle\sigma_{ij}\rangle_V||$ of the cell-averaged Cauchy stress tensor for the both the DNS results and the homogenization results, respectively, where

$$\langle\sigma_{ij}\rangle_V \doteq \frac{1}{V}\int_V \sigma_{ij}(\mathbf{x},\mathbf{y})\,dV\ , \tag{3.54}$$

and V represents the volume of the unit cell. Figure 3.9c shows the magnitude of the difference of the cell-averaged Cauchy stress, $||\langle\sigma_{ij}^{\mathrm{DNS}}\rangle_V - \langle\sigma_{ij}^{\mathrm{H}}\rangle_V||$. The difference is about 2 %.

3.3.4 Computational Homogenization

Typically, the solution of the cell problem given by Eq. (3.37) requires a numerical approximation in all but the simplest cases, as was demonstrated in Sect. 3.3.3. For linear materials, the cell problem is only solved once to obtain the homogenized material properties. These homogenized material properties can then be used in any boundary-value problem consistent with the assumptions of the homogenization. For inelastic problems, the deformation of the unit cell is typically history dependent, and thus cannot be homogenized *a priori* in general. Instead, the homogenization step must be performed concurrently during the simulation of the macroscale problem [75]. Within a finite-element framework, each macroscale finite element has a unit cell (or RVE) embedded within each integration point. For the displacement-based finite-element method, the host code sends an increment of deformation to the material model, and the material model sends back an increment of stress. This concurrent-multiscale process is sometimes referred to as "computational homogenization," or $(\text{FE})^2$ (finite element squared), since a finite-element model is active at the macroscale and at the microscale (unit cell). This computational approach is analogous to the *local* quasi-continuum method discussed within Chap. 6 of this book. Fish [50] has developed a general-purpose multiscale software [94] that includes several computational homogenization capabilities.

For first-order homogenization, the main assumption is the presence of a scale separation between the microscale and macroscale, $l/L \ll 1$, where now the macroscopic length scale L should take into account strain gradients as well. The assumption of a scale separation and small strain gradients typically breaks down when the material localizes, such as when shear-banding and fracture occur. The range of applicability of computational homogenization can be extended by including strain-gradient effects (higher-order homogenization theory) [32, 33, 54, 76, 149].

While the unit-cell problem defined by Eq. (3.37) can be solved using standard numerical techniques, such as the finite-element method, a very efficient numerical algorithm has been developed by Moulinec and Suquet [107] based on the FFT. This approach transforms the set of partial-differential equations with periodic boundary conditions into a convolution-based integral equation that can be solved using fixed-point iteration in Fourier space. The FFT method for solving the unit-cell problem has proven effective for both linear and nonlinear computational homogenization [97, 98, 107]. Eisenlohr et al. [43] have compared the finite-element solution of the unit-cell problem to the FFT method for polycrystals in the large deformation regime. Massively parallel implementations of the FFT algorithm exist in three dimensions [122] as well as GPU implementations [99].

To set up the FFT-based fixed-point iteration algorithm, the concept of a linear homogeneous reference medium with stiffness tensor $\mathbf{C}_0$ is introduced, along with the polarization stress $\boldsymbol{\tau}$ defined by

$$\boldsymbol{\tau}(\mathbf{y}) = \boldsymbol{\sigma}(\mathbf{y}) - \mathbb{C}_0 : \boldsymbol{\epsilon}(\mathbf{y}) = (\mathbb{C}(\mathbf{y}) - \mathbb{C}_0) : \boldsymbol{\epsilon}(\mathbf{y}) \,. \tag{3.55}$$

Equation (3.37) can be cast in the form of the periodic Lippmann–Schwinger equation,

$$\boldsymbol{\epsilon}(\mathbf{y}) = -\int_V \boldsymbol{\Gamma}_0(\mathbf{y},\mathbf{y}') : \boldsymbol{\tau}(\mathbf{y}')\, d\mathbf{y}' + \mathbf{E}, \tag{3.56}$$

where $\boldsymbol{\Gamma}_0(\mathbf{y},\mathbf{y}')$ is a fourth-order tensor related to the Green's function of the homogeneous reference medium [109], and here $\mathbf{E}$ represents a constant strain over the unit cell. Taking the Fourier transform of Eq. (3.56) turns the nonlocal convolution in real space into a local product in Fourier space,

$$\hat{\boldsymbol{\epsilon}}(\boldsymbol{\xi}) = -\widehat{\Gamma}_0(\boldsymbol{\xi}) : \hat{\boldsymbol{\tau}}(\boldsymbol{\xi}) \quad \text{for all } \boldsymbol{\xi} \neq \mathbf{0} \tag{3.57a}$$

$$\hat{\boldsymbol{\epsilon}}(\mathbf{0}) = \mathbf{E}\,, \tag{3.57b}$$

where $\boldsymbol{\xi}$ is the spatial frequency vector. In Fourier space, $\widehat{\Gamma}_0(\boldsymbol{\xi})$ is given explicitly by

$$\widehat{\Gamma}_{klij}(\boldsymbol{\xi}) = \frac{\delta_{ki}\xi_l\xi_j + \delta_{li}\xi_k\xi_j + \delta_{kj}\xi_l\xi_i + \delta_{lj}\xi_k\xi_i}{4\mu_o||\boldsymbol{\xi}||^2} - \frac{\lambda_o + \mu_o}{\mu_o(\lambda_o + 2\mu_o)}\frac{\xi_i\xi_j\xi_k\xi_l}{||\boldsymbol{\xi}||^4}\,, \tag{3.58}$$

where λ_0 and μ_0 are the Lame coefficients of the reference medium, and δ_{ij} is the Kronecker delta.

Since the polarization stress defined in Eq. (3.55) is a function of the unknown strain field $\boldsymbol{\epsilon}(\mathbf{x})$, an iterative solution of Eq. (3.57) can be obtained using the fixed-point scheme

$$\hat{\boldsymbol{\epsilon}}^{i+1}(\boldsymbol{\xi}) = -\widehat{\Gamma}_0(\boldsymbol{\xi}) : \hat{\boldsymbol{\tau}}^{i}(\boldsymbol{\xi}) \quad i = 0, 1, 2, \ldots\,. \tag{3.59}$$

The steps in this algorithm are shown in Fig. 3.10. The convergence test in the algorithm measures the deviation from equilibrium (divergence of stress equal to zero) within a given tolerance. Note that the algorithm does not involve the solution of a matrix equation. According to Banach's fixed-point theorem [77], the fixed-point iteration converges to a unique solution if the operator implicit in Eq. (3.56) is a contraction. This condition has been studied extensively, and can be assured under certain restrictions for λ_0 and μ_0 [98]. The number of iterations required for convergence scales with the ratio of maximum and minimum contrasts in the elastic moduli. For a nonlinear material, only step 6 needs to be modified to return the stress for the given value of strain. For a history-dependent material, an incremental version of the algorithm is used [43].

The development of numerical schemes that accelerate the basic FFT algorithm is an active area of research. Recent improvements include using a periodic Green's operator instead of one based on an infinite medium [20, 21, 70, 98, 156].

Initialization :
$$\boldsymbol{\varepsilon}^0(\mathbf{y}) = \mathbf{E}\,, \quad \text{for all } \mathbf{y} \in V$$
$$\boldsymbol{\sigma}^0(\mathbf{y}) = \mathbb{C}(\mathbf{y}) : \boldsymbol{\varepsilon}^0(\mathbf{y})\,, \quad \text{for all } \mathbf{y} \in V$$

Iteration $i+1$: with $\boldsymbol{\varepsilon}^i$ and $\boldsymbol{\sigma}^i$ known

1. $\boldsymbol{\tau}^i(\mathbf{y}) = \boldsymbol{\sigma}^i(\mathbf{y}) - \mathbb{C}_0 : \boldsymbol{\varepsilon}^i(\mathbf{y})$
2. $\hat{\boldsymbol{\tau}}^i(\boldsymbol{\xi}) = \mathcal{F}(\boldsymbol{\tau}^i(\mathbf{y}))$
3. convergence test
4. $\hat{\boldsymbol{\varepsilon}}^{i+1}(\boldsymbol{\xi}) = -\widehat{\Gamma}_0(\boldsymbol{\xi}) : \hat{\boldsymbol{\tau}}^i(\boldsymbol{\xi}) \quad \text{for all } \boldsymbol{\xi} \neq \mathbf{0}\,, \quad \hat{\boldsymbol{\varepsilon}}^{i+1}(\mathbf{0}) = \mathbf{E}$
5. $\hat{\boldsymbol{\varepsilon}}^{i+1}(\mathbf{x}) = \mathcal{F}^{-1}(\boldsymbol{\varepsilon}^{i+1}(\boldsymbol{\xi}))$
6. $\boldsymbol{\sigma}^{i+1}(\mathbf{y}) = \mathbb{C}(\mathbf{y}) : \boldsymbol{\varepsilon}^{i+1}(\mathbf{y})$

Fig. 3.10 Iterative FFT algorithm for solving the homogenization unit-cell problem given by Eq. (3.37) [107]. $\mathscr{F}$ represents the FFT (in 3D), and $\mathscr{F}^{-1}$ represents the inverse FFT (in 3D). The convergence test measures the deviation from equilibrium

3.4 Crystal-Plasticity Models

In many macroscale constitutive models, phenomenological formulations are developed for specific classes of materials such as those for plasticity and viscoplasticity (polycrystalline metals) [74, 83, 87, 111], hyperelasticity and viscoelasticity (polymers) [29], and pressure dependent plasticity (porous materials) [5, 19]. These models use various internal-state variables to phenomenologically model physical effects such as dislocation slip, dislocation density, porosity, and damage. Through these constitutive models, the stress is related to the entire history of deformation. Constitutive models also exist that describe the deformation of the grain or single-crystal scale in metals by incorporating homogenization of discrete dislocation slip events [127]. These constitutive models are generally referred to as "crystal plasticity" (CP) models. Some CP models use dislocation densities explicitly as internal-state variables, and thus incorporate additional length scales [15]. In this section, crystal-plasticity models based on a continuum approximation will be discussed as one class of inelastic continuum model.

3.4.1 Background

Crystal-plasticity models are based on single-crystal plastic deformation via dislocation motion through a crystal lattice on specific slip systems. The applied stress is resolved onto predefined slip systems to accommodate plastic deformation of each grain or crystal. Figure 3.11 illustrates the Schmid law, $\tau = \sigma \cos\lambda \cos\phi$, that defines the relationship between the shear stress τ resolved on the slip plane and the uniaxial applied stress σ. Here, ϕ is the angle between the slip plane with normal $\mathbf{n}$ and the loading axis, and λ is the angle between the slip direction $\mathbf{m}$ and

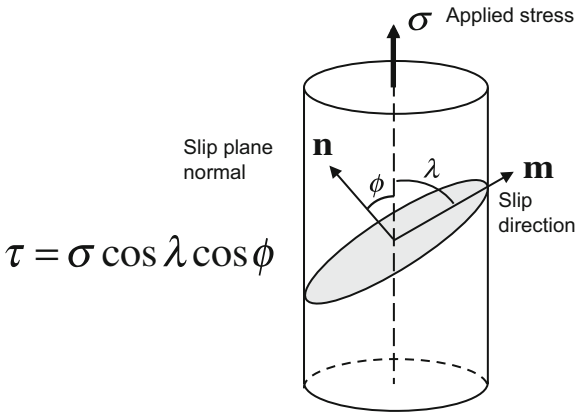

Fig. 3.11 Schematics of the Schmid law. The resolved shear stress τ is described by the applied stress σ, cosine of the angle ϕ between the slip-plane normal **n** and the loading axis, and cosine of the angle λ between the slip direction **m** and the loading axis

the loading axis. For the case of arbitrary loading, τ can be represented using a contraction between the Schmid tensor, $\mathbf{P} = 1/2(\mathbf{m} \otimes \mathbf{n} + \mathbf{n} \otimes \mathbf{m})$, and the applied stress tensor, $\boldsymbol{\sigma}$.

With some simplifying assumptions of the interactions between grains, single-crystal constitutive equations can be used to directly approximate the response of a polycrystal. Classical polycrystal plasticity models (texture models) assume simplified interactions between grains, e.g., the same stress state [132] or strain state [145] for each crystal. However, these models ignore intergranular compatibility and equilibrium, respectively. Recently, crystal-plasticity constitutive models implemented within nonlinear displacement-based finite-element (FEM) codes enforce compatibility strongly and equilibrium weakly. In addition to solving the equilibrium equations, the advantages of crystal-plasticity FEM (CP-FEM) include the ability to handle irregular shaped domains, complex boundary conditions, and multiple material phases. Furthermore, high performance computers enable simulations of polycrystalline domains on macroscopic length scales, i.e., having millions of grains. Polycrystalline simulations using CP-FEM can provide mechanical properties of the polycrystalline body with consideration of microstructural effects such as texture evolution (crystal orientations), multi-phases, defects (voids and dislocations), and grain morphology (shapes and sizes).

The basic assumptions used in conventional crystal-plasticity models are (1) the deformation gradient can be decomposed into elastic and plastic parts, and (2) plastic deformation occurs by dislocation slip on the predefined slip systems. Thus, conventional crystal-plasticity models ignore other deformation mechanisms such as cross slip, climb, dislocation twinning, grain-boundary sliding, and non-Schmid yield behavior. More sophisticated models have been developed to capture these effects [71, 86, 89]. In this section, the most widely adopted crystal-plasticity formulation by Peirce et al. [121] is outlined.

3.4.2 Model Formulations

Crystal-plasticity models generally adopt a multiplicative decomposition of the deformation gradient $\mathbf{F}$ into elastic $\mathbf{F}^{\mathrm{e}}$ and plastic $\mathbf{F}^{\mathrm{p}}$ parts [62, 82, 121, 126],

$$\mathbf{F} = \mathbf{F}^{\mathrm{e}}\,\mathbf{F}^{\mathrm{p}} \,. \tag{3.60}$$

As the crystal deforms, the lattice is rotated and elastically stretched and sheared according to $\mathbf{F}^{\mathrm{e}}$. The plastic deformation gradient $\mathbf{F}^{\mathrm{p}}$ is calculated from the crystal slip as [9]:

$$\mathbf{F}^{\mathrm{p}} = \mathbf{I} + \sum_{\alpha} \gamma^{\alpha} \mathbf{s}_0^{\alpha} \otimes \mathbf{n}_0^{\alpha} \,, \tag{3.61}$$

where γ^{α} is the amount of slip in α slip system, $\mathbf{s}_0^{\alpha}$ and $\mathbf{n}_0^{\alpha}$ are the unit vectors in the slip direction and slip-plane normal direction on the α slip system in the original configuration, respectively, and $\mathbf{I}$ is the identity tensor. The slip systems for different crystal structures, FCC and BCC, are given in Table 3.2.

The velocity gradient in the current configuration, $\mathbf{L} \doteq \partial \mathbf{v}/\partial \mathbf{x}$, can be written as

$$\mathbf{L} = \dot{\mathbf{F}}\,\mathbf{F}^{-1} = \mathbf{L}^{\mathrm{e}} + \mathbf{L}^{\mathrm{p}} \,, \tag{3.62}$$

Table 3.2 Slip systems for different crystal structures

α	Slip system	α	Slip system	α	Slip system	α	Slip system
Twelve FCC slip systems							
1	$(01\bar{1})[111]$	4	$(0\bar{1}\bar{1})[\bar{1}\bar{1}1]$	7	$(01\bar{1})[\bar{1}\bar{1}\bar{1}]$	10	$(0\bar{1}\bar{1})[11\bar{1}]$
2	$(\bar{1}01)[111]$	5	$(101)[\bar{1}\bar{1}1]$	8	$(\bar{1}01)[\bar{1}\bar{1}\bar{1}]$	11	$(101)[11\bar{1}]$
3	$(1\bar{1}0)[111]$	6	$(\bar{1}10)[\bar{1}\bar{1}1]$	9	$(1\bar{1}0)[\bar{1}\bar{1}\bar{1}]$	12	$(\bar{1}10)[11\bar{1}]$
Twenty four {110} *BCC slip systems*							
1	$(01\bar{1})[111]$	7	$(0\bar{1}\bar{1})[\bar{1}\bar{1}1]$	13	$(01\bar{1})[\bar{1}\bar{1}\bar{1}]$	19	$(0\bar{1}\bar{1})[11\bar{1}]$
2	$(\bar{1}01)[111]$	8	$(101)[\bar{1}\bar{1}1]$	14	$(\bar{1}01)[\bar{1}\bar{1}\bar{1}]$	20	$(101)[11\bar{1}]$
3	$(1\bar{1}0)[111]$	9	$(\bar{1}10)[\bar{1}\bar{1}1]$	15	$(1\bar{1}0)[\bar{1}\bar{1}\bar{1}]$	21	$(\bar{1}10)[11\bar{1}]$
4	$(\bar{1}0\bar{1})[\bar{1}11]$	10	$(10\bar{1})[1\bar{1}1]$	16	$(\bar{1}0\bar{1})[1\bar{1}\bar{1}]$	22	$(10\bar{1})[\bar{1}1\bar{1}]$
5	$(0\bar{1}1)[\bar{1}11]$	11	$(011)[1\bar{1}1]$	17	$(0\bar{1}1)[1\bar{1}\bar{1}]$	23	$(011)[\bar{1}1\bar{1}]$
6	$(110)[\bar{1}11]$	12	$(\bar{1}\bar{1}0)[1\bar{1}1]$	18	$(110)[1\bar{1}\bar{1}]$	24	$(\bar{1}\bar{1}0)[\bar{1}1\bar{1}]$
Twenty four {112} *BCC slip systems*							
1	$(11\bar{2})[111]$	7	$(\bar{1}\bar{1}2)[\bar{1}\bar{1}1]$	13	$(11\bar{2})[\bar{1}\bar{1}\bar{1}]$	19	$(\bar{1}\bar{1}2)[11\bar{1}]$
2	$(\bar{2}11)[111]$	8	$(2\bar{1}1)[\bar{1}\bar{1}1]$	14	$(\bar{2}11)[\bar{1}\bar{1}\bar{1}]$	20	$(2\bar{1}1)[11\bar{1}]$
3	$(1\bar{2}1)[111]$	9	$(\bar{1}21)[\bar{1}\bar{1}1]$	15	$(1\bar{2}1)[\bar{1}\bar{1}\bar{1}]$	21	$(\bar{1}21)[11\bar{1}]$
4	$(\bar{1}1\bar{2})[\bar{1}11]$	10	$(1\bar{1}2)[1\bar{1}1]$	16	$(\bar{1}1\bar{2})[1\bar{1}\bar{1}]$	22	$(1\bar{1}2)[\bar{1}1\bar{1}]$
5	$(\bar{1}2\bar{1})[\bar{1}11]$	11	$(121)[1\bar{1}1]$	17	$(\bar{1}2\bar{1})[1\bar{1}\bar{1}]$	23	$(121)[\bar{1}1\bar{1}]$
6	$(211)[\bar{1}11]$	12	$(\bar{2}\bar{1}1)[1\bar{1}1]$	18	$(211)[1\bar{1}\bar{1}]$	24	$(\bar{2}\bar{1}1)[\bar{1}1\bar{1}]$

where $\mathbf{L}^{\mathrm{e}}$ and $\mathbf{L}^{\mathrm{p}}$ are elastic and plastic parts of the velocity gradient, respectively, and are given by

$$\mathbf{L}^{\mathrm{e}} = \dot{\mathbf{F}}^{\mathrm{e}} \left(\mathbf{F}^{\mathrm{e}}\right)^{-1} \quad \text{and} \quad \mathbf{L}^{\mathrm{p}} = \mathbf{F}^{\mathrm{e}} \dot{\mathbf{F}}^{\mathrm{p}} \left(\mathbf{F}^{\mathrm{p}}\right)^{-1} \left(\mathbf{F}^{\mathrm{e}}\right)^{-1} . \tag{3.63}$$

The plastic part of the velocity gradient $\mathbf{L}^{\mathrm{p}}$ is given as [121]

$$\mathbf{L}^{\mathrm{p}} = \sum_{\alpha} \dot{\gamma}^{\alpha} \, \mathbf{s}_0^{\alpha} \otimes \mathbf{n}_0^{\alpha} , \tag{3.64}$$

where $\dot{\gamma}^{\alpha}$ is the slip rate on the α slip system.

The critical aspect of single-crystal constitutive equations is formulating how the slip rate is related to the applied stress. The most widely used form for a viscoplastic formulation is based on the power-law function [66, 126],

$$\dot{\gamma} = \dot{\gamma}_0 \left(\frac{\tau}{g}\right)^{1/m} \mathrm{sign}(\tau) , \tag{3.65}$$

where $\dot{\gamma}_0$ is the reference shear rate, m is the rate sensitivity, and g is the slip resistance. Alternatively, the slip rate can be modeled using a thermal activation form given by Ma et al. [89].

$$\dot{\gamma} = \dot{\gamma}_0 \exp\left[-\frac{Q}{kT}\left(1 - \frac{\tau}{g}\right)\right] \mathrm{sign}(\tau) , \tag{3.66}$$

where Q is the activation enthalpy, k is the Boltzmann constant, and T is temperature. This form is useful when the crystal slip exhibits large temperature dependence, e.g., for body-centered cubic (BCC) crystal structure.

The slip resistance g represents strain hardening. There are different models for g, e.g., isotropic hardening, slip-based hardening, or dislocation density-based hardening. Classical isotropic hardening models generally assume that all slip systems harden equally as a function of plastic strain [88]. Slip-based hardening models are also widely used in crystal-plasticity models, and have been used to successfully predict texture and anisotropic behaviors in polycrystals [72, 91]. In slip-based hardening models, the strain hardening term is related to the slip increment on all slip systems through the relation [8],

$$\dot{g}^{\alpha} = \sum_{\beta} h^{\alpha\beta} |\dot{\gamma}^{\alpha}| . \tag{3.67}$$

Here, $h^{\alpha\beta}$ is the hardening matrix that relates hardening on one slip system to other active slip systems. Different hardening matrices that account for anisotropy and dislocation–dislocation interactions have been proposed [13, 38, 52, 79]. The widely used form that successfully predicts stress–strain behavior of polycrystals is as follows [22]:

$$h^{\alpha\beta} = \mathbf{q}^{\alpha\beta} h_0 \left(1 - \frac{g^{\beta}}{g_s}\right)^{a} . \tag{3.68}$$

Here, h_0 is the initial hardening rate, g_s is the saturated flow stress, and a is the hardening exponent. $\mathbf{q}^{\alpha\beta}$ is a hardening matrix that determines the self to latent hardening ratios. The diagonal terms of $\mathbf{q}^{\alpha\beta}$, denoted by q_{self}, describe self-hardening while the non-diagonal terms denoted by q_{lat} describe the latent hardening effect. The values $q_{\text{self}} = 1$ and $q_{\text{lat}} = 1.4$ are commonly used in polycrystalline simulations [10, 91, 121].

The dislocation density-based Taylor hardening law is represented as follows [144]:

$$g = A\mu b \sqrt{\sum_{\beta=1} \rho^{\beta}} \,, \tag{3.69}$$

where A is a material constant, μ is the shear modulus, b is the Burger's vector (magnitude), and ρ^{β} is the dislocation density on slip system β. The evolution of dislocation density for the α slip system is obtained by a standard phenomenological equation [73],

$$\dot{\rho}^{\alpha} = \left(\kappa_1 \sqrt{\sum_{\beta=1}^{24} \rho^{\beta}} - \kappa_2 \rho^{\alpha} \right) \cdot |\dot{\gamma}^{\alpha}| \,, \tag{3.70}$$

where κ_1 and κ_2 are hardening parameters representing generation and annihilation of dislocations, respectively, and ultimately determine the shape of the stress–strain curve.

Other variations of crystal-plasticity models include different types of time integration schemes, e.g., implicit or explicit, as well as rate independent models. Crystal-plasticity constitutive models can be implemented within the standard finite-element formulation [127]. This is commonly done in commercial software such as ABAQUS [1] and ANSYS [6], as well as more specialized finite-element software such as ALBANY [4], DAMASK [37, 129], and ZEBULON [155].

3.4.3 CP and Nanomechanics

One of the strengths of the crystal-plasticity model is that it can accommodate microstructure in simulations and provides realistic length and time scales. Modern CP-FEM has been modified and applied to various micro- to grain-scale problems [128]:

- Texture evolution, plastic anisotropy
- Nonlocal formulations, grain boundary mechanics, grain size effects
- Metal forming, deep drawing, springback
- Surface roughening, ridging, roping.
- Damage and fracture, fatigue, void growth

- Micromechanics: nanoindentation, micropillar testing
- Creep, high temperature deformation, diffusion mechanisms
- Deformation twinning, martensitic transformation, shape memory, phase transformation, recrystallization

There are two main limitations in applying conventional CP models directly to nanoscale materials. First, as grain sizes are reduced to nanometer sizes in nanocrystalline materials, the assumption of a continuous dislocation density becomes increasingly suspect. Second, many experiments and lower length-scale simulation results show that conventional dislocation plasticity in non-nanocrystalline metals breaks down in nanoscale materials. For example, discrete dislocation grain-boundary interactions and grain boundary sliding become significant deformation mechanisms at this scale. Note that conventional CP models do not properly incorporate these effects. To overcome these limitations, advanced CP models have appeared in the literature [53, 84, 85, 153]. They either use quantized slip or incorporate grain boundary effects to capture deformation mechanisms at the nanoscale. More detailed description of the quantized crystal-plasticity (QCP) model is discussed in Chap. 13.

3.5 Conclusions

In this chapter, we have briefly reviewed continuum mechanics, homogenization theory, computational homogenization, and constitutive modeling including crystal-plasticity. Our review of continuum mechanics included an overview of micromorphic and nonlocal theories as well as continuum formulations that include an explicit surface stress. At the center of continuum mechanics is homogenization theory which provides a mathematically elegant and rigorous framework for replacing a discrete collection of interacting entities by an equivalent homogenous continuum with effective material properties. Numerous references to much more detailed expositions on these topics were provided throughout the chapter.

Errors in a continuum approximation to a discrete system are unavoidable whenever the introduced length scales are comparable to the length scale of the discrete system. Generalized continuum theories may be able to reproduce qualitatively correct physical phenomenon, such as a surface effect or optical-branch phonon dispersion curves, but the accuracy of the continuum theory must be judged with respect to the true behavior of the original discrete system.

Appendix

Example: Error in the Continuum Approximation

Discrete systems have an inherent length scale governed fundamentally by the interaction distance between entities. The accuracy of the continuum approximation depends critically on the size of the structure compared to the size of this intrinsic length scale. To illustrate the continuum approximation of a discrete system and its accuracy, consider a simple one-dimensional chain of N atoms of total initial length L with initial atomic spacing l subjected to a body force F per atom as shown in Fig. 3.12a. The initial position X_I of each atom is given by $X_I = l \cdot I$, $I = 0, 1, 2, 3, \ldots, N$ with $X_N = L$. For simplicity, we take the interatomic potential to be harmonic with spring constant K, pair-wise additive, with only nearest-neighbor interactions.

The forces between the atoms are linear with respect to the relative displacements so that

$$K(u_N - u_{N-1}) = F \tag{3.71a}$$

$$K(u_{N-1} - u_{N-2}) = 2F \tag{3.71b}$$

$$\vdots$$

$$K(u_I - u_{I-1}) = F(N - I + 1) \tag{3.71c}$$

$$\vdots$$

$$K(u_1 - u_0) = FN \tag{3.71d}$$

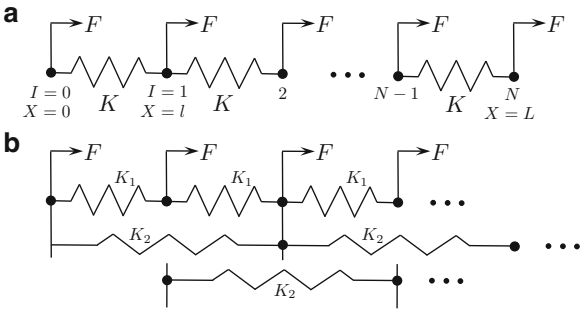

Fig. 3.12 (**a**) One-dimensional chain of atoms of total initial length L with initial atomic spacing l subjected to a body force F per atom. The initial position X_I of each atom is given by $X_I = l \cdot I$, $I = 0, 1, 2, 3, \ldots, N$ with $X_N = L$. The interatomic forces are governed by *local* interactions and a spring constant K. (**b**) One-dimensional chain of atoms with *nonlocal* interatomic forces. The nearest-neighbor spring constant is K_1, and next-nearest spring constant is K_2

where u_I is the displacement of atom I with $u_0 = 0$. Since this set of equations telescopes starting with $u_1 = FN/K$, we have

$$u_I = \frac{F}{K}\left[I \cdot N - \sum_{J=1}^{I}(J-1)\right] = \frac{F}{K}\left[I \cdot N - \frac{1}{2}I(I-1)\right]. \tag{3.72}$$

Since $N = L/l$ and $I = X_I/l$, we can write Eq. (3.72) as

$$u_I = \frac{(F/l)L^2}{(Kl)}\left[\frac{X_I}{L}\left(1 + \frac{l}{2L}\right) - \frac{1}{2}\left(\frac{X_I}{L}\right)^2\right]. \tag{3.73}$$

Note that the natural length-scale ratio for this problem is l/L.

To obtain the continuum version of this problem, we first use Eq. (3.13) reduced to the one-dimensional form, along with a linear-elastic constitutive model, $\sigma_{xx} = Edu/dX$. This results in the following equation for the continuum displacement field in a one-dimensional bar,

$$\frac{d}{dX}\left(k\frac{du}{dX}\right) + f(X) = 0\,, \tag{3.74}$$

where f is the body force per unit length along the bar, and k is the cross-sectional stiffness. The solution to this equilibrium equation with the boundary condition $u(0) = 0$ is given by

$$u(X) = \frac{fL^2}{k}\left[\frac{X}{L} - \frac{1}{2}\left(\frac{X}{L}\right)^2\right]. \tag{3.75}$$

Note that there is no intrinsic length scale in this continuum solution. If we identify $k = K \cdot l$ and $F = f \cdot l$, then Eq. (3.73) converges to Eq. (3.75) in the limit as $l/L \to 0$. The absolute error in the continuum approximation is given by,

$$e_I \doteq |u(X_I) - u_I| = \frac{fL^2}{k}\left(\frac{X_i}{L}\right)\left(\frac{l}{2L}\right) \tag{3.76}$$

This error is proportional to the length-scale ratio l/L. Also, the error varies linearly along the chain, from $e_0 = 0$ at $X_0 = 0$ to a maximum value at $X_N = 0$. Thus, in the limit of infinitesimally small intrinsic length scale, the discrete solution converges to the continuum solution.

The normalized displacement solution for the discrete atom chain, given by Eq. (3.73) with $\bar{u} \doteq u/(FL^2/Kl^2)$, is shown in Fig. 3.13a as a function of normalized initial position, $\bar{X} \doteq X/L$, for several values of the length-scale ratio l/L. The continuum approximation for the displacement field, given by Eq. (3.75), is also shown. The error in the continuum approximation, given by Eq. (3.76) with $\bar{e} \doteq |\bar{u} - \bar{u}_I|$, is shown in Fig. 3.13b, and is seen to approach zero as $l/L \to 0$. Only for $l/L < 0.02$ ($N = 50$) is the maximum error less than 2 % of the peak displacement.

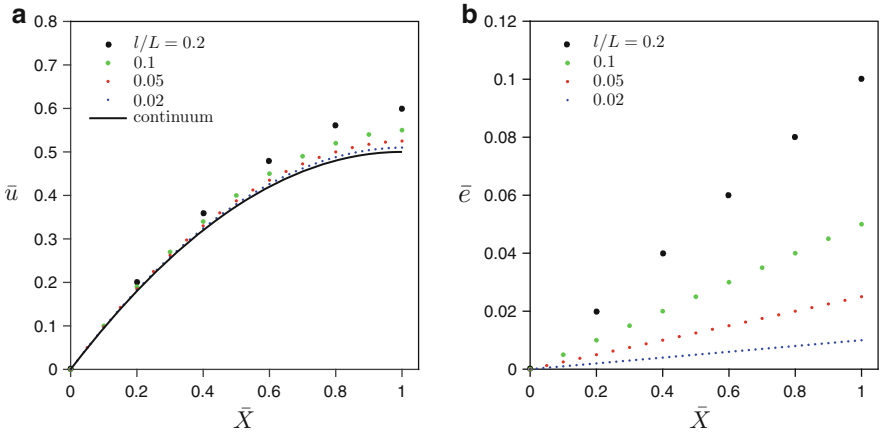

Fig. 3.13 (**a**) Normalized displacement $\bar{u}$ as a function of normalized initial position $\bar{X}$ of a one-dimensional chain of atoms subjected to a uniform body force and fixed at the end $\bar{X} = 0$ for various values of the ratio of atom spacing to total initial chain length, l/L. The continuum approximation is also shown. (**b**) Normalized error in the continuum approximation. Only for $l/L < 0.02$ ($N = 50$) is the maximum error less than 2 % of the peak displacement

Example: Absence of a Surface Effect in Classical Continuum Mechanics

Discrete systems can also display surface effects that are not present in classical continuum theories. To illustrate the continuum approximation of a discrete system and its accuracy, consider a simple one-dimensional chain of N atoms of total initial length L with initial atomic spacing l subjected to a body force F per atom as shown in Fig. 3.12b. The initial position X_I of each atom is given by $X_I = l \cdot I$, $I = 0, 1, 2, 3, \ldots, N$ with $X_N = L$. We take the interatomic potential to be harmonic, pair-wise additive, with both nearest-neighbor interactions with spring constant K_1, and nonlocal interactions with spring constant K_2. Note that the atoms at the end of the chain experience a distinctly different force environment than those atoms in the interior of the chain due to the number of interacting neighbors.

The forces between the atoms are linear with respect to the relative displacements so that

$$K_1(u_N - u_{N-1}) + K_2(u_N - u_{N-2}) = F \quad (3.77a)$$

$$-K_1(u_N - u_{N-1}) + K_1(u_{N-1} - u_{N-2}) + K_2(u_{N-1} - u_{N-3}) = F \quad (3.77b)$$

$$-K_2(u_N - u_{N-2}) - K_1(u_{N-1} - u_{N-2}) + K_1(u_{N-2} - u_{N-3}) + K_2(u_{N-2} - u_{N-4}) = F \quad (3.77c)$$

$$\vdots$$

$$-K_2(u_{I+2} - u_I) - K_1(u_{I+1} - u_I) + K_1(u_I - u_{I-1}) + K_2(u_I - u_{I-2}) = F \quad (3.77d)$$

$$\vdots$$

$$-K_2(u_3 - u_1) - K_1(u_2 - u_1) + K_1(u_1 - u_0) = F \quad (3.77e)$$

where u_I is the displacement of atom I with $u_0 = 0$. This system of equations results in a matrix equation $\mathbf{Ku} = \mathbf{F}$ where $\mathbf{K}$ is $N \times N$ banded matrix of the Toeplitz type and can be solved using standard methods.

The normalized displacement solution for the discrete atom chain with $\bar{u} \doteq u/(FL^2/K_1 l^2)$ is shown in Fig. 3.14a as a function of normalized initial position, $\bar{X} \doteq X/L$, for several values of the length-scale ratio l/L. For this example, we have chosen $K_2 = 0.5K_1$. In order to use the continuum approximation given by Eq. (3.75), we must first define an effective spring stiffness, K_{eff}. To this end, we isolate a unit cell of length $2l$ surrounding one *interior* atom. Within each cell, there are two K_1 springs acting in series thus contributing a value of $\frac{1}{2}K_1$ to K_{eff}. There is a full K_2 spring acting in parallel thus contributing a value of K_2 to K_{eff}. There are also two K_2 springs that effectively act in parallel to the unit cell, thus contributing a value of $\frac{1}{2}K_2 + \frac{1}{2}K_2$ to K_{eff}. Thus, $K_{\text{eff}} = \frac{1}{2}K_1 + 2K_2$, and $k \doteq K_{\text{eff}} \cdot (2l)$. Also, the effective force per unit length is $f = 2F/2l = F/l$. The continuum approximation

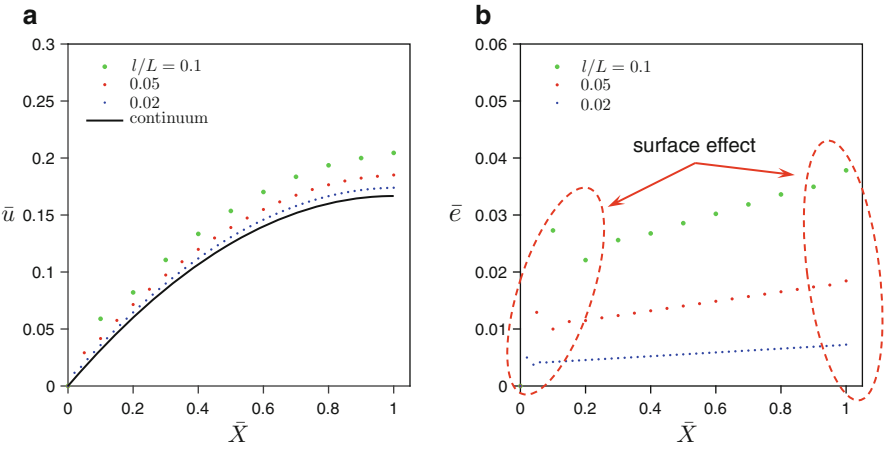

Fig. 3.14 Illustration of the surface effect for a one-dimensional discrete chain of atoms subjected to a body force F applied to each atom. The atoms are connected to their nearest neighbors by linear springs with spring constant K_1, and to their next-nearest neighbors by linear springs with spring constant K_2. The chain is fixed at $X = 0$. The total initial length of the chain is L, and the atomic spacing is l so that the number of atoms $N = L/l$. (**a**) Normalized displacement, $\bar{u} \doteq u/(FL^2/K_1 l^2)$, plotted as a function of the normalized initial position, $\bar{X} \doteq X/L$. Results are shown for $l/L = 0.1, 0.05, 0.02$ ($N = 10, 20, 50$, respectively) with $K_2 = 0.5K_1$. The continuum approximation, $l/L \to 0$, is also shown with $\bar{u} \doteq u/(fL^2/k)$ where $f \doteq F/l$, and $k \doteq K_1\, l$. (**b**) Error in the continuum approximation with $\bar{e} \doteq |\bar{u} - \bar{u}_i|$

for the displacement field is also shown in Fig. 3.14a. There is some noticeable surface effect on the atoms near the ends of the chain, particularly near $\bar{X} = 0$. This effect is more noticeable if we plot the error in the continuum approximation, $\bar{e} \doteq |\bar{u} - \bar{u}_I|$, as shown in Fig. 3.14b. Notice that the surface effect near $\bar{X} = 0$ affects several atoms. The surface effect is absent in the chosen continuum approximation.

Acknowledgements Sandia National Laboratories is a multi-program laboratory operated by Sandia Corporation, a wholly owned subsidiary of Lockheed Martin Corporation, for the US Department of Energy's National Nuclear Security Administration under contract DE-AC04-94AL85000.

References

1. ABAQUS, http://www.3ds.com/products-services/simulia/products/abaqus/ (2015)
2. E. Aifantis, Update on a class of gradient theories. Mech. Mater. **35**(3–6), 259–280 (2003)
3. E. Aifantis, On the gradient approach – relation to Eringen's nonlocal theory. Int. J. Eng. Sci. **49**(12), 1367–1377 (2011)
4. ALBANY, https://github.com/gahansen/Albany (2015)
5. A. Anandarajah, *Computational Methods in Elasticity and Plasticity: Solids and Porous Media* (Springer, New York, 2010)
6. ANSYS, http://www.ansys.com (2015)
7. B. Arash, Q. Wang, A review on the application of nonlocal elastic models in modeling of carbon nanotubes and graphenes. Comput. Mater. Sci. **51**(1), 303–313 (2012)
8. R.J. Asaro, Geometrical effects in the inhomogeneous deformation of ductile single crystals. Acta. Metall. **27**, 445 (1979)
9. R.J. Asaro, Micromechanics of crystals and polycrystals. Adv. Appl. Mech. **23**, 1–115 (1983)
10. R.J. Asaro, A. Needleman, Texture development and strain hardening in rate dependent polycrystals. Acta Metall. **33**, 923–953 (1985)
11. J. Auriault, G. Bonnet, Surface effects in composite materials: two simple examples. Int. J. Eng. Sci. **25**(3), 307–323 (1987)
12. J. Barber, *Elasticity* (Springer, New York, 2010)
13. J.L. Bassani, T.Y. Wu, Latent hardening in single crystals II. Analytical characterization and predictions. Proc. R. Soc. Lond. A. **435**, 21–41 (1991)
14. G. Beer, I. Smit, C. Duenser, *The Boundary Element Method with Programming* (Springer, Wien, 2008)
15. T. Belytschko, W. Liu, B. Moran, K. Elkhodary, *Nonlinear Finite Elements for Continua and Structures*, 2nd edn. (Wiley, London, 2014)
16. A. Bensoussan, J. Lions, G. Papanicolaou, *Asymptotic Analysis for Periodic Structures* (American Mathematical Society, Providence, 2011)
17. F. Bobaru, Influence of van der Waals forces on increasing the strength and toughness in dynamic fracture of nanofibre networks: a peridynamic approach. Model. Simul. Mater. Sci. Eng. **15**(5), 397–417 (2007)
18. J. Bonet, R. Wood, *Nonlinear Continuum Mechanics for Finite Element Analysis*, 2nd edn. (Cambridge University Press, Cambridge, 2008)
19. A. Bower, *Applied Mechanics of Solids* (CRC, New York, 2010)
20. S. Brisard, L. Dormieux, FFT-based methods for the mechanics of composites: a general variational framework. Comput. Mater. Sci. **49**(3), 663–671 (2010)
21. S. Brisard, L. Dormieux, Combining Galerkin approximation techniques with the principle of Hashin and Shtrikman to derive a new FFT-based numerical method for the homogenization of composites. Comput. Methods Appl. Mech. Eng. **217–220**, 197–212 (2012)

22. S.B. Brown, K.H. Kim, L. Anand, An internal variable constitutive model for hot working of metals. Int. J. Plast. **5**, 95–130 (1989)
23. H. Butt, M. Kappl, *Surface and Interfacial Forces*, 3rd edn. (Wiley-VCH, Weinheim, 2010)
24. H. Butt, K. Graf, M. Kappl, *Physics and Chemistry of Interfaces*, 3rd edn. (Wiley-VCH, Weinheim, 2013)
25. Y. Chen, J. Lee, Connecting molecular dynamics to micromorphic theory. (I). Instantaneous and averaged mechanical variables. Phys. A Stat. Mech. Appl. **322**, 359–376 (2003)
26. Y. Chen, J. Lee, Determining material constants in micromorphic theory through phonon dispersion relations. Int. J. Eng. Sci. **41**(8), 871–886 (2003)
27. Y. Chen, J. Lee, A. Eskandarian, Examining the physical foundation of continuum theories from the viewpoint of phonon dispersion relation. Int. J. Eng. Sci. **41**(1), 61–83 (2003)
28. Y. Chen, J. Lee, A. Eskandarian, Atomistic viewpoint of the applicability of microcontinuum theories. Int. J. Solids Struct. **41**(8), 2085–2097 (2004)
29. R. Christensen, *Theory of Viscoelasticity: An Introduction*, 2nd edn. (Academic, New York, 1982)
30. D. Cioranescu, P. Donato, *An Introduction to Homogenization* (Oxford University Press, Oxford, 1999)
31. A. Cleland, *Foundations of Nanomechanics: From Solid-State Theory to Device Applications* (Springer, New York, 2003)
32. E. Coenen, V. Kouznetsova, M. Geers, Enabling microstructure-based damage and localization analyses and upscaling. Model. Simul. Mater. Sci. Eng. **19**(7), 074,008 (2011)
33. E. Coenen, V. Kouznetsova, M. Geers, Novel boundary conditions for strain localization analyses in microstructural volume elements. Int. J. Numer. Methods Eng. **90**(1), 1–21 (2012)
34. COMSOL Multiphysics, http://www.comsol.com (2015)
35. E. Cosserat, *Theorie des Corps Deformable* (Hermann, Paris, 1909)
36. CUBIT Geometry and Meshing Toolkit, https://cubit.sandia.gov (2012)
37. DAMASK, http://damask.mpie.de (2015)
38. B. Devincre, L. Kubin, Scale transitions in crystal plasticity by dislocation dynamics simulations. C. R. Phys. **11**, 274–284 (2010)
39. F. Devries, H. Dumontet, G. Duvaut, F. Lene, Homogenization and damage for composite structures. Int. J. Numer. Methods Eng. **27**, 285–298 (1989)
40. R. Dingreville, J. Qu, M. Cherkaoui, Surface free energy and its effect on the elastic behavior of nano-sized particles, wires and films. J. Mech. Phys. Solids **53**, 1827–1854 (2005)
41. H. Dumontet, Study of a boundary layer problem in elastic composite materials. Math. Model. Numer. Anal. **20**(2), 265–286 (1987)
42. M. Duzzi, M. Zaccariotto, U. Galvanetto, Application of peridynamic theory to nanocomposite materials. Adv. Mater. Res. **1016**, 44–48 (2014)
43. P. Eisenlohr, M. Diehl, R. Lebenshohn, F. Roters, A spectral method solution to crystal elasto-viscoplasticity at finite strains. Int. J. Plast. **46**, 37–53 (2013)
44. J. Ericksen, On the Cauchy-Born rule. Math. Mech. Solids **13**, 199–200 (2008)
45. A. Eringen, *Microcontinuum Field Theories I: Foundations and Solids* (Springer, New York, 1999)
46. A. Eringen, *Nonlocal Continuum Field Theories* (Springer, New York, 2002)
47. A. Eringen, D. Edelen, On nonlocal elasticity. Int. J. Eng. Sci. **10**(3), 233–248 (1972)
48. A. Eringen, E. Suhubi, Nonlinear theory of simple microelastic solids – I. Int. J. Eng. Sci. **2**(2), 189–203 (1964)
49. E. Eringen, E. Oterkus, *Peridynamic Theory and its Applications* (Springer, New York, 2014)
50. J. Fish, *Practical Multiscaling* (Wiley, Chichester, 2014)
51. N. Fleck, J. Hutchinson, Strain gradient plasticity. Adv. Appl. Mech. **33**, 295–361 (1997)
52. P. Franciosi, A. Zaoui, Multislip in F.C.C crystals: a theoretical approach compared with experimental data. Acta Metall. **30**, 1627 (1982)
53. H. Fu, D.J. Benson, M.A. Meyers, Computational description of nanocrystalline deformation based on crystal plasticity. Acta Mater. **52**, 4413–4425 (2004)

54. M. Geers, V. Kouznetsova, W. Brekelmans, Multi-scale computational homogenization: trends and challenges. J. Comput. Appl. Math. **234**(7), 2175–2182 (2010)
55. P. Germain, The method of virtual power in continuum mechanics. part 2: microstructure. SIAM J. Appl. Math. **25**(3), 556–575 (1973)
56. S. Gonella, M. Greene, W. Liu, Characterization of heterogeneous solids via wave methods in computational microelasticity. J. Mech. Phys. Solids **59**, 959–974 (2011)
57. M. Gurtin, A. Murdoch, Addenda to our paper a continuum theory of elastic material surfaces. Arch. Ration. Mech. Anal. **59**(4), 389–390 (1975)
58. M. Gurtin, A. Murdoch, A continuum theory of elastic material surfaces. Arch. Ration. Mech. Anal. **57**(4), 291–323 (1975)
59. M. Gurtin, A. Murdoch, Surface stress in solids. Int. J. Solids Struct. **14**, 431–440 (1978)
60. M. Gurtin, J. Weissmuller, F. Larche, A general theory of curved deformable interfaces in solids at equilibrium. Philos. Mag. A **78**(5), 1093–1109 (1998)
61. L. He, Z. Li, Impact of surface stress on stress concentration. Int. J. Solids Struct. **43**, 6208–6219 (2006)
62. R. Hill, J.R. Rice, Constitutive analysis of elastic plastic crystals at arbitrary strain. J. Mech. Phys. Solids **20**, 401–413 (1972)
63. M. Holmes, *Introduction to Perturbation Methods*, 2nd edn. (Springer, New York, 2013)
64. G. Holzapfel, *Nonlinear Solid Mechanics: A Continuum Approach for Engineering* (Wiley, New York, 2000)
65. C. Huet, Application of variational concepts to size effects in elastic heterogeneous bodies. J. Mech. Phys. Solids **38**(6), 813–841 (1990)
66. J.W. Hutchinson, Bounds and self-consistent estimates for creep of polycrystalline materials. Proc. R. Soc. Lond. A **348**, 101–127 (1976)
67. H. Ibach, The role of surface stress in reconstruction, epitaxial growth and stabilization of mesoscopic structures. Surf. Sci. Rep. **29**, 193–263 (1997)
68. V. Jikov, S. Kozlov, O. Oleinik, *Homogenization of Differential Operators and Integral Functionals* (Springer, New York, 1994)
69. M. Jirásek, Nonlocal models for damage and fracture: comparison of approaches. Int. J. Solids Struct. **35**(31–32), 4133–4145 (1998)
70. M. Kabel, D. Merkert, M. Schneider, Use of composite voxels in FFT-based homogenization. Comput. Methods Appl. Mech. Eng. **294**, 168–188 (2015)
71. S.R. Kalidindi, Incorporation of deformation twinning in crystal plasticity models. J. Mech. Phys. Solids **46**, 267–290 (1998)
72. S.R. Kalidindi, C.A. Bronkhorst, L. Anand, Crystallographic texture evolution in bulk deformation processing of FCC metals. J. Mech. Phys. Solids **40**, 537 (1992)
73. U.F. Kocks, Laws for work-hardening and low-temperature creep. ASME J. Eng. Mater. Tech. **98**, 76–85 (1976)
74. U. Kocks, C. Tome, H. Wenk (eds.), *Texture and Anisotropy: Preferred Orientations in Polycrystals and Their Effect on Material Properties* (Cambridge University Press, New York, 1998)
75. V. Kouznetsova, W. Brekelmans, F. Baaijens, An approach to micro-macro modeling of heterogeneous materials. Comput. Mech. **27**(1), 37–48 (2001)
76. V. Kouznetsova, M. Geers, W. Brekelmans, Multi-scale constitutive modelling of heterogeneous materials with a gradient-enhanced computational homogenization scheme. Int. J. Numer. Methods Eng. **54**(8), 1235–1260 (2002)
77. E. Kreysig, *Introductory Functional Analysis with Applications* (Wiley, New York, 1978)
78. E. Kröner, Elasticity theory of materials with long range cohesive forces. Int. J. Solids Struct. **3**(5), 731–742 (1967)
79. L. Kubin, B. Devincre, T. Hoc, Modeling dislocation storage rates and mean free paths in face-centered cubic crystals. Acta Mater. **56**, 6040–6049 (2008)
80. LAMMPS, Molecular dynamics simulator. http://lammps.sandia.gov (2015)
81. H. Ledbetter, Monocrystal-polycrystal elastic constants of a stainless steel. Phys. Status Solidi A **85**(1), 89–96 (1984)

82. E.H. Lee, Elastic-plastic deformation at finite strains. Appl. Mech. **36**, 1–6 (1969)
83. J. Lemaitre, J. Chaboche, *Mechanics of Solid Materials* (Cambridge University Press, Cambridge, 1990)
84. L. Li, P.M. Anderson, M.G. Lee, E. Bitzek, P. Derlet, H.V. Swygenhoven, The stress-strain response of nanocrystalline metals: A quantized crystal plasticity approach. Acta Mater. **57**, 812–822 (2009)
85. L. Li, M.G. Lee, P.M. Anderson, Critical strengths for slip events in nanocrystalline metals: predictions of quantized crystal plasticity simulations. Metall. Mater. Trans. A Phys. Metall. Mater. Sci. **42**, 3875–3882 (2011)
86. H. Lim, C.R. Weinberger, C.C. Battaile, T.E. Buchheit, Application of generalized non-Schmid yield law to low temperature plasticity in BCC transition metals. Model. Simul. Mater. Sci. Eng. **21**, 045,015 (2013)
87. J. Lubliner, *Plasticity Theory* (Macmillan Publishing Company, New York, 1990)
88. P. Ludwik, *Element der Technologischen Mechanik* (Springer, New York, 1909)
89. A. Ma, F. Roters, D. Raabe, A dislocation density based constitutive law for BCC materials in crystal plasticity FEM. Comp. Mat. Sci. **39**, 91–95 (2007)
90. L. Malvern, *Introduction to the Mechanics of a Continuous Medium* (Prentice-Hall, Englewood Cliffs, 1969)
91. K.K. Mathur, P.R. Dawson, On modeling the development of crystallographic texture in bulk forming processes. Int. J. Plast. **5**, 67–94 (1989)
92. C. McVeigh, W. Liu, Linking microstructure and properties through a predictive multiresolution continuum. Comput. Methods Appl. Mech. Eng. **197**, 3268–3290 (2008)
93. C. McVeigh, W. Liu, Multiresolution continuum modeling of micro-void assisted dynamic adiabatic shear band propagation. J. Mech. Phys. Solids **58**, 187–205 (2010)
94. MDS: Multiscale Design Systems, http://multiscale.biz (2015)
95. C. Mei, B. Vernescu, *Homogenization Methods for Multiscale Mechanics*, 2nd edn. (World Scientific, New York, 2010)
96. C. Mi, D. Kouris, Nanoparticles under the influence of surface/interface elasticity. J. Mech. Mater. Struct. **1**(4), 763–791 (2006)
97. J. Michel, H. Moulinec, P. Suquet, Effective properties of composite materials with periodic microstructure: a computational approach. Comput. Methods Appl. Mech. Eng. **172**(1–4), 109–143 (1999)
98. J. Michel, H. Moulinec, P. Suquet, Comparison of three accelerated FFT-based schemes for computing the mechanical response of composite materials. Int. J. Numer. Methods Eng. **97**, 960–985 (2014)
99. B. Mihaila, M. Knezevic, A. Cardenas, Three orders of magnitude improved efficiency with high-performance spectral crystal plasticity on GPU platforms. Int. J. Numer. Methods Eng. (2014)
100. R. Miller, V. Shenoy, Size-dependent elastic properties of nanosized structural elements. Nanotechnology **11**, 139–147 (2000)
101. R. Mindlin, Influence of couple-stresses on stress concentrations. Exp. Mech. **3**(1), 1–7 (1963)
102. R. Mindlin, Micro-structure in linear elasticity. Arch. Ration. Mech. Anal. **16**(1), 51–78 (1964)
103. R. Mindlin, Second gradient of strain and surface-tension in linear elasticity. Int. J. Solids Struct. **1**, 417–438 (1965)
104. R. Mindlin, N. Eshel, On first strain-gradient theories in linear elasticity. Int. J. Solids Struct. **4**, 109–124 (1968)
105. R. Mindlin, H. Tiersten, Effects of couple-stresses in linear elasticity. Arch. Ration. Mech. Anal. **11**(1), 415–448 (1962)
106. T. Mori, K. Tanaka, Average stress in matrix and average elastic energy of materials with misfitting inclusions. Acta Metall. **21**(5), 571–574 (1973)
107. H. Moulinec, P. Suquet, A numerical method for computing the overall response of nonlinear composites with complex microstructure. Comput. Methods Appl. Mech. Eng. **157**(1–2), 69–94 (1998)

108. P. Muller, A. Saul, Elastic effects on surface physics. Surf. Sci. Rep. **54**, 157–258 (2004)
109. T. Mura, *Micromechanics of Defects in Solids* (Martinus Nijhoff Publishers, The Hague, 1982)
110. S. Nemat-Nasser, M. Hori, *Micromechanics: Overall Properties of Heterogeneous Materials*, 2nd edn. (Elsevier, Amsterdam, 1999)
111. A. Nowick, B. Berry, *Anelastic Relaxation in Crystalline Solids* (Academic, New York,1972)
112. G. Papanicolaou, S. Varadhan, Boundary value problems with rapidly oscillating random coefficients. Colloquia Math. Soc. J'anos Bolyai **27**, 835–873 (1979)
113. H. Park, P. Klein, A surface cauchy-born analysis of surface stress effects on metallic nanowires. Physical Review B **75**, 085,408:1–9 (2007)
114. H. Park, P. Klein, G. Wagner, A surface cauchy-born model for nanoscale materials. Int. J. Numer. Methods Eng. **68**, 1072–1095 (2006)
115. M. Parks, R. Lehoucq, S. Plimpton, S. Silling, Implementing peridynamics within a molecular dynamics code. Comput. Phys. Commun. **179**(11), 777–783 (2008)
116. M. Parks, S. Plimpton, R. Lehoucq, S. Silling, Peridynamics with LAMMPS: a user guide. Technical Report, SAND 2008-1035, Sandia National Laboratories (2008). http://www.sandia.gov/~mlparks
117. G. Pavliotis, A. Stuart, *Multiscale Methods: Averaging and Homogenization* (Springer, New York, 2008)
118. J. Peddieson, G. Buchanan, R. McNitt, Application of nonlocal continuum models to nanotechnology. Int. J. Eng. Sci. **41**(3–5), 305–312 (2003)
119. R. Peerlings, N. Fleck, Computational evaluation of strain gradient elasticity constants. Int. J. Multiscale Comput. Eng. **2**(4), 599–619 (2004)
120. R. Peerlings, M. Geers, R. de Borst, W. Brekelmans, A critical comparison of nonlocal and gradient-enhanced softening continua. Int. J. Solids Struct. **38**(44–45), 7723–7746 (2001)
121. D. Peirce, R.J. Asaro, A. Needleman, An analysis of nonuniform and localized deformation in ductile single crystals. Acta Metall. **30**, 1087–1119 (1982)
122. D. Pekurovsky, P3DFFT: A framework for parallel computations of Fourier transforms in three dimensions. SIAM J. Sci. Comput. **34**(4), C192–C209 (2012)
123. C. Polizzotto, Nonlocal elasticity and related variational principles. Int. J. Solids Struct. **38**(42–43), 7359–7380 (2001)
124. C. Polizzotto, Unified thermodynamic framework for nonlocal/gradient continuum theories. Eur. J. Mech. A. Solids **22**(5), 651–668 (2003)
125. P. Seleson, M. Parks, M. Gunzburger, R. Lehoucq, Peridynamics as an upscaling of molecular dynamics. Multiscale Model. Simul. **8**(1), 204–227 (2009)
126. J.R. Rice, Inelastic constitutive relations for solids, an internal-variable theory and its application to metal plasticity. J. Mech. Phys. Solids **19**, 443–455 (1971)
127. F. Roters, P. Eisenlohr, T. Bieler, D. Raabe, *Crystal Plasticity Finite Element Methods in Materials Science and Engineering* (Wiley-VCH, Berlin, 2010)
128. F. Roters, P. Eisenlohr, L. Hantcherli, D. Tjahjanto, T. Bieler, D. Raabe, Overview of constitutive laws, kinematics, homogenization and multiscale methods in crystal plasticity finite-element modeling: theory, experiments, applications. Acta Mater. **58**, 1152–1211 (2010)
129. F. Roters, P. Eisenlohr, C. Kords, D. Tjahjanto, M. Diehl, D. Raabe, DAMASK: the Düsseldorf Advanced MAterial Simulation Kit for studying crystal plasticity using an FE based or a spectral numerical solver. Proc. IUTAM **3**, 3–10 (2012)
130. A. Rusanov, Surface thermodynamics revisited. Surf. Sci. Rep. **58**, 111–239 (2005)
131. A. Rusanov, Surface thermodynamics of cracks. Surf. Sci. Rep. **67**, 117–140 (2012)
132. G. Sachs, Ableitung einer fliessbedingung. Z. Ver. Dtsch. Ing. **72**, 734–736 (1928)
133. E. Sanchez-Palencia, *Non-Homogeneous Media and Vibration Theory*. Lecture Notes in Physics, vol. 127 (Springer, New York, 1980)
134. P. Sharma, S. Ganti, Size-dependent Eshelby's tensor for embedded nano-inclusions incorporating surface/interface energies. J. Appl. Mech. **71**, 663–671 (2004)
135. V. Shenoy, R. Miller, E. Tadmor, D. Rodney, R. Phillips, M. Ortiz, An adaptive finite element approach to atomic-scale mechanics–the quasicontinuum method. J. Mech. Phys. Solids **47**, 611–642 (1999)

136. S. Silling, Reformulation of elasticity theory for discontinuities and long-range forces. J. Mech. Phys. Solids **48**(1), 175–201 (2000)
137. S. Silling, R. Lehoucq, Peridynamic theory of solid mechanics. Adv. Appl. Mech. **44**, 74–164 (2010)
138. S. Silling, M. Epton, O. Weckner, J. Xu, E. Askari, Peridynamic states and constitutive modeling. J. Elast. **88**(2), 151–184 (2007)
139. V. Smyshlyaev, K. Cherednichenko, On rigorous derivation of strain gradient effects in the overall behaviour of periodic heterogeneous media. J. Mech. Phys. Solids **48**, 1325–1357 (2000)
140. E. Suhubi, A. Eringen, Nonlinear theory of simple microelastic solids – II. Int. J. Eng. Sci. **2**(4), 389–404 (1964)
141. E. Tadmor, M. Ortiz, R. Phillips, Quasicontinuum analysis of defects in solids. Philos. Mag. A **73**(6), 1529–1563 (1996)
142. E. Tadmor, G. Smith, N. Bernstein, E. Kaxiras, Quasicontinuum analysis of defects in solids. Phys. Rev. B **59**(1), 235–245 (1999)
143. Tahoe Development Project, http://tahoe.sourceforge.net (2015)
144. G.I. Taylor, The mechanism of plastic deformation of crystals. Part I. Theoretical. Proc. R. Soc. A **165**, 362–387 (1934)
145. G.I. Taylor, Plastic strain in metals. J. Inst. Metals **62**, 307–324 (1938)
146. S. Timoshenko, J. Goodier, *Theory of Elasticity*, 3rd edn. (McGraw-Hill, New York, 1987)
147. R. Toupin, Elastic materials with couple-stresses. Arch. Ration. Mech. Anal. **11**(1), 385–414 (1962)
148. R. Toupin, Theories of elasticity with couple-stress. Arch. Ration. Mech. Anal. **17**(2), 85–112 (1964)
149. T. Tran, V. Monchiet, G. Bonnet, A micromechanics-based approach for the derivation of constitutive elastic coefficients of strain-gradient media. Int. J. Solids Struct. **49**(5), 783–792 (2012)
150. F. Vernerey, W. Liu, B. Moran, Multi-scale micromorphic theory for hierarchical materials. J. Mech. Phys. Solids **55**, 2603–2651 (2007)
151. Q. Wang, K. Liew, Application of nonlocal continuum mechanics to static analysis of micro- and nano-structures. Phys. Lett. A **363**(3), 236–242 (2007)
152. J. Wang, Z. Huang, H. Duan, S. Yu, X. Feng, G. Wang, W. Zhang, T. Wang, Surface stress effect in mechanics of nanostructured materials. Acta Mech. Solida Sin. **24**(1), 52–82 (2011)
153. D.H. Warner, J.F. Molinari, A semi-discrete and non-local crystal plasticity model for nanocrystalline metals. Scr. Mater. **54**, 1397–1402 (2006)
154. X. Yuan, Y. Tomita, T. Andou, A micromechanical approach of nonlocal modeling for media with periodic microstructures. Mech. Res. Commun. **35**(1–2), 126–133 (2008)
155. ZEBULON, http://www.nwnumerics.com/Zebulon/ (2015)
156. J. Zeman, J. Vondřejc, J. Novák, I. Marek, Accelerating a FFT-based solver for numerical homogenization of periodic media by conjugate gradients. J. Comput. Phys. **229**(21), 8065–8071 (2010)